Graduate thesis

NTNU
Norwegian University of Science and Technology
Faculty of Natural Sciences
Department of Physics

Andreas Andersen Hennig

Statistical Properties of a Single-Phase Bingham Fluid in Porous Media

Graduate thesis in Applied Physics and Mathematics (MTFYMA)
Supervisor: Alex Hansen
Co-supervisor: Laurent Talon
June 2023

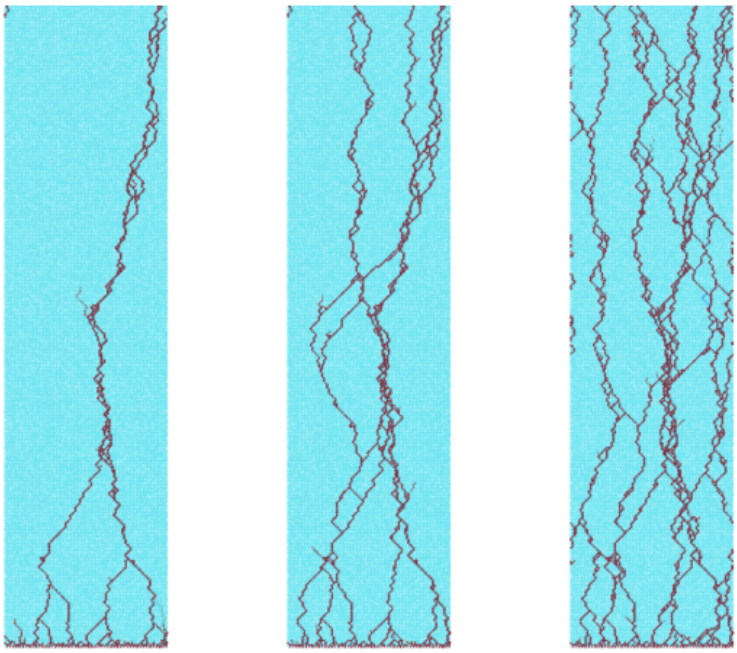

NTNU
Norwegian University of
Science and Technology

Andreas Andersen Hennig

Statistical Properties of a Single-Phase Bingham Fluid in Porous Media

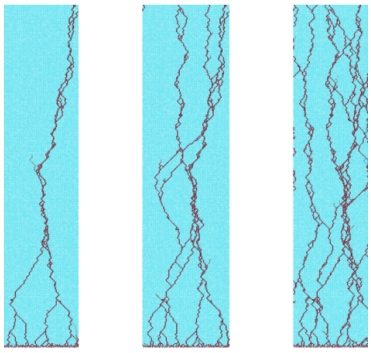

Graduate thesis in Applied Physics and Mathematics (MTFYMA)
Supervisor: Alex Hansen
Co-supervisor: Laurent Talon
June 2023

Norwegian University of Science and Technology
Faculty of Natural Sciences
Department of Physics

NTNU
Norwegian University of
Science and Technology

Preface

This work concludes my journey through the 5 year programme in applied physics and mathematics at NTNU in Trondheim. These years were a real adventure, and the people I've met throughout these years has been exceptional people with all their passion, determination, humour and quirk. I will never forget the feeling of belonging the first day we met with our study programme, and I've truly been right where I should be for these 5 years.

This last year has been quite crazy, and my first acknowledgement goes to my supervisor, Alex Hansen for giving me these amazing opportunities to venture out into the big world of science during my year at PoreLab. Not all master students gets to go 3 months abroad, present at an international conference, participate at workshops and meeting all these amazing researchers, and I am truly lucky to have had you supervising this project.

A major acknowledgement goes to Laurent Talon of Université Paris-Saclay who had the role as my second supervisor, and I would like to express my gratitude for your time, devotion and friendliness, much needed for a small-town Norwegian's first meeting with Paris. I had a great and productive time in France, and I've thoroughly enjoyed all our discussions and cooperation.

There are so many other people to thank too! I want to thank soon-to-be-dr. Federico Lanza for all your help this year. I have benefitted a lot from your discussions, and I've had so much fun – both in Oslo, in Paris and especially in Edinburgh! A big thanks to the whole PoreLab office for interesting coffee breaks and discussions, and especially the other Master's students at PoreLab for all our shenanigans this last year, ranging from board games and Mario Party to hour-long table-tennis sessions – your company will be missed. I'd like to thank the PoreLab group in Oslo for giving me and Federico such a warm welcome and great supervision when we went to visit for the experimental study. Furthermore, I am grateful for all the discussions with Kristoffer Moen – your enthusiasm for fluid dynamics is infectious to say the least!

My family has backed me up so many times throughout the years, and although I'm never able to explain what I've been doing, you have always cheered on me. Especially the company of my sister, Martine[1], has been important these 5 years, and it is amazing to see that the two of us actually did what we sat out to do (and so much more) 5 years ago!

Finally I would like to thank my girlfriend Elle for all your love and support throughout these 5 years. Meeting you is best thing that has happened to me, and I'm truly grateful for all your patience and kindness.

Now let's say what Alex usually says after the initial chit-chat: *Now let's talk science!*

[1] Usually referred to as Olga

Disclaimer to the examiner

During evaluation, part II and part III are the only parts to be evaluated as the Master's thesis. This structure is chosen in order to avoid self-plagiarism of the project thesis, which I wanted to include for completeness, as the project thesis works as the preliminaries for the Master's thesis. Some of the key concepts and equations will be repeated in part II, making the text complete and readable in itself – however, I would recommend any reader to go through both parts, as part II is constantly referring to equations, figures and concepts in part I.

Abstract

Part I (Project thesis): The effect of a Yield Stress Rheology in a Porous Media

Two phase flows are complex phenomena that occurs everywhere from the stroke of a pen to the extraction of ground water, having a great importance in a wide array of engineering applications. Their inner workings has been studied for decades, and the field has heavily involved both a mathematical, geological, chemical and physical perspective. However, the effects of *yield stress rheologies* in a two phase flow are still far from understood. Solving these systems on useful scales is very computationally expensive, hence sophisticated modeling is required to analyse the system-size behaviors. Yield stress rheologies are present in many commonly encountered fluids, pastes and muds, with applications in industries and everyday life. In this work, a pore-network model is implemented with a recently developed Agumented Lagrangian Method, making it possible to study the system-size effects with a nonlinear rheology in reasonable time. The effect of the yield stress is modeled as a Bingham fluid and can be studied for various flow rates, surface tensions, geometries and yield stresses. The results show that the network simulator is capable of reproducing some of the existing Newtonian results, indicating that the simulator runs successfully. For increasing yield stresses we get very different patterns and behaviors, and the immobilized fluid forms interesting patterns that are discussed qualitatively. A power-law relation between the system threshold pressure and imposed flow rate was finally found in a single phase Bingham flow, demonstrating that the simulator reproduces known yield stress effects as well. The Agumented Lagrangian Method has proved useful in effectively solving the system equations, and the modeling allows for varying a wide range of parameters and their interplay with the yield stress rheology. Hence, further work will be focused on systematically vary the most relevant parameters, and to characterize the flow patterns both qualitatively and quantitatively in the goal of making a phase diagram analogous to the Newtonian ones available in literature, using tools from statistical physics.

Part II (Master thesis): Statistical Properties of a Single-Phase Bingham Fluid in Porous Media

Single-phase Bingham fluids in porous media are complex systems not well understood, yet with immediate utility both in industry and in scientific measurements. They exhibit a striking similarity to magnetic flux lines in high-T_c superconductors, with the same underlying structure: both will have directed preferential paths through the system, making highways through the disordered landscape. These are examples of the directed polymer in random media, and a ground state minimizing the pressures associated to yield the Bingham fluids is defined. In the ground state, paths merge with a certain rate, corresponding to the roughness of the directed polymer; the remaining immobilized fluid can be divided into clusters, whose probability density function (PDF) follow a power-law as $p(S) \propto Q^{-\tau}$ with exponent $\tau = 1.4$. The ground state is then used to understand the transition observed towards a fully flowing system, looking at the cluster size PDF, evolution of branches, and finally the effective permeability of the flow state, behaving in a

non-Darcy way. A stable number of branches, n_0 is found, and is shown to give the same scaling properties for two-phase Bingham flows; indeed, yield stress dominant two-phase flows exhibit several similarities to their single-phase counterparts. For instance, the transition from a directed polymer ground state into a fully mobilized network was also found in a special case in the two-phase Bingham flows. The amount of branches and characteristics of immobilized clusters are believed to make good measures for characterizing and understanding the complex and unexplored field of two-phase flows in porous media with yield stress rheologies.

Oppsummering

Del I (Prosjektoppgave): Effekten av en Terskelstress-Reologi på Strømninger i Porøse Medier

Tofasestrømmer i porøse medier er komplekse fenomener som foregår over alt, fra et delikat pennestrøk til utvinning av grunnvann finner man slike systemer. De er viktige til flere praktiske formål, og dets indre mekanismer har blitt omhyggelig studert og forsket på i flere tiår. Fagfeltet står sentralt i både matematikk, geologi, kjemi og fysikk, og må kunne kalles tverrfaglig. Effekten av terskelstressreologi i en tofasestrømning er dog ikke viden kjent, og de er utfordrende å se på numerisk, da det å løse ligningene eksakt vil være svært beregningstungt – det krever flittig modellering for å ha sjans på å studere noen størrelse av betydning. Disse terskelstressreologiene finner vi blant annet i gjørmer og pastaer, og har anvendelser i en god del hverdagslige produkter, som tannkrem, for eksempel. I dette arbeidet implementerer vi en *Agumented Lagrangian Method* (ALM) i en porenettverksmodell (PNM) som gjør det mulig å se på systemstørrelser av disse ikkelinære reologiene. Effekten av terskelstress modelleres på enkleste vis som en Bingham-fluid, og kan simuleres for ønskede verdier av strømningsrate, overflatespenning, geometrier og terskelstress. Resultatene viser at nettverksmodellen er i stand til å reprodusere noen kjente resultater for vanlige, Newtonske fluider, som ble brukt til å teste dens troverdighet. Økende terskelstress gir kvalitativt veldig ulike mønstre og oppførsler, blant annet ved en potenslov mellom strømningen gjennom mediet og trykkfallet gjennom – dette fungerer som enda en test på at ALM-løseren fungerer som den skal. Dermed er alt lagt til rette for å undersøke effektene av de mest relevante parameterene som vi kan styre ved simuleringene, i et forsøk på å lage et resulterende fasediagram av hva som skjer.

Del II (Masteroppgave): Statistiske Egenskaper i en Énfase Bingham-Fluid Strømning i Porøse Medier

Énfase Binghamfluider i porøse medier er kompliserte systemer som ikke er fullt forstått, men som likevel har umiddelbar nytte både for industri og for videre forskning. Vi har en slående likhet med magnetiske flukslinjer i type-II høytemperaturs-superledere, på grunn av en lignende underliggende struktur: Begge vil ha foretrukne veier gjennom det uordnede landskapet de skal gjennom. Dette er igjen eksempler på *Directed Polymers in Random Media* (DPRM), og vi definerer en grunntilstand som minimerer trykkfallet fra terkselstressene over hele systemet. I denne grunntilstanden vil de åpne veiene i nettverket slå seg sammen, hvor sannsynligheten for at to veier slår seg sammen er den samme som ruheten i DPRM. Resten av det urørlige Binghamfluidet vil holde seg i klynger, hvis fordeling blir funnet til å passe med en potenslov $p(S) \propto Q^{-\tau}$ med $\tau = 1.4$. Grunntilstanden brukes så til å forstå overgangen mot et fullt strømmende system, hvor vi ser på klyngefordelingene, utviklingen av strømmende veier gjennom systemet, og til slutt den effektive permeabiliteten til strømningen i nettverksmodellen, som ikke oppfører seg på den vanlige "Darcy-strømning"-måten. Et stabilt antall strømmende grener i nettverket, n_0, defineres, noe vi finner igjen når vi ser på tofase-Binghamstrømninger gjennom nettverket. Terskelstressdominerte tofasestrømmer har flere likheter med deres énfase motpart, ek-

sempelvis finner vi igjen en overgang fra en DPRM-type strømning til et fullt strømmende nettverk ved noen spesielle tilfeller. Antallet strømmende grener og klyngestørrelser egner seg til å karakterisere og forstå dette komplekse og uoppdagede forskningsfeltet innen tofasestrømmer med terkselstressreologi i porøse medier.

Table of Contents

Part I

The Effect of a Yield Stress Rheology in a Porous Media

(Project thesis)

1

Introduction

Fluids flowing through porous media, specific as it may sound, occur everywhere in nature and in everyday life. From rainwater seeping down the soil, to making a coffee in the morning; we encounter these kinds of flows more often than we might think, and understanding their processes is of great importance for a large variety of applications.

For instance, consider the ink that flows from a pen onto a sheet of paper. This is a real engineering merit, designed in such a delicate way that the ink flows perfectly into the pores of the paper: not too much so the ink bleeds through the other side of the paper, nor too little, so that the writing would not make smooth reliable lines – the perfect balance between ink viscosity, ink flow rate, paper permeability and paper thickness. These delicate instruments of pen and paper help us think, communicate and document our findings to new generations – without it we would not have neither Newtons *Principia* nor Shakespeares sonnets. Forget the wheel, the printing press and the computer – the invention of the pen and paper thrones as the most important in the evolution of society, and is done by engineering a flow through a porous media.

However, engineering flows through porous media isn't only used in such archaic inventions as the pen; in fact, they are of vital importance in many recent inventions, for instance in the porous electrodes in a fuel cell [1]. Estimation and retrieval of groundwater is another challenge related to porous media flows, which will be of vital importance in solving the water scarcity affecting an estimated 4 billion people at least 1 month a year [2], a problem addressed as one of the UN's 19 sustainable development goals. Storing liquefied CO2 is another porous media problem to be solved for the coming generations, which is currently investigated and attempted by the porous media group of the University in Bergen, among others [3].

However, the underlying physics governing flows through porous media are still not fully understood, and we are lacking any generalized theory predicting both small scale and kilometer scale behavior. Generally the most used law – the Darcy law – relies on a phenomenological proportionality constant, and is only valid for certain scales, hence lacking theoretical explanations. The language of statistical mechanics has proved useful in explaining some of the many phenomena, for instance in the critical behavior of

percolation [4].

In the digital age, we have a chance of studying these complex behaviors at scales that demand computational prowess. Since the birth of computational physics, people have been studying these complex systems, hunting for statistical properties and characterising their behaviors, making for new theories and frameworks [5, 6].

As the statistician George Box famously stated in 1976 *"All models are wrong, but some are useful"*. The assumption of Newtonian fluids is a good example of a useful model, as it applies for some of the most important fluids we encounter like water and air, but there are exceptions, which are called Non-Newtonian fluids. These have a non-linear relation between shear stress and shear rate – a nonlinear viscosity – and some are even time-dependent. There are several non-Newtonian fluids of great importance – our own blood, for instance [7].

There are several ways of modeling different non-Newtonian fluids, and one of the simpler models are so-called Bingham fluids[1], capturing the yield stress effect in a non-Newtonian rheology. The yield stress effect is the characteristic that separates a lump of honey to a lump of mayonnaise: The honey will slowly spread out, while the mayonnaise will stay in place, and needs an external stress to start flowing. Indeed the effect describes something inbetween a fluid and a solid, and according to [8], the whole field of rheology started when Eugene C. Bingham investigated concentrated clay suspensions, in parallel to working on oilpaints with Green in a work 1919 titled *"Paint, a Plastic Material and not a Viscous Liquid"*. In both works he saw the necessity to parture from classical hydrodynamics, creating the Bingham fluid model and inspiring the birth of a whole field.

This Bingham-fluid-model is useful in modeling several important fluids, such as foams, slurries, drilling muds, heavy oils, and clay suspensions [9, 10] which has found engineering applications in soil reinforcement and in fracking processes [10]. Interestingly enough, yield stress effects can also be found in several foods, like ketchup, peanut butter and cookie cream [11], so these fluids are commonly encountered in everyday life.

This thesis is structured in the following form:

In chapter 2 we give an introduction to two-phase Newtonian flow in porous media, introducing the physical concepts, resulting patterns and decisions on modeling.

Chapter 3 is dedicated to Bingham fluids, how they behave and on how to implement the nonlinear rheology numerically.

Finally, in chapter 4 we summarize and conclude our findings, proposing an outlook for further investigations for the following master thesis.

[1] Sometimes referred to as a Bingham plastic or a Bingham body.

2

Two-Phase Flow in Porous Media

2.1 Darcy's law

When working on water supply systems in the french city of Dijon in the 1850s, Henry Darcy published the famous Darcy law for water flow through porous media, where he found the flow rate proportional to the pressure difference he imposed on his experimental setup [12]. The proportionality constant K was found to be dependent on the viscosity of the fluid μ, but also dependent on the *permeability*, k, which is a characteristic of the porous medium. This permeability can be modeled and calculated, for instance with the Carman-Kozeny equation, which relates the permeability with the porosity of the porous media – the larger the pore-sizes, the easier it is for the fluid to flow through.

Darcy's law, disregarding the gravitational term and inertial effects, can be formulated as

$$Q = -\frac{k}{\mu A}\nabla p, \tag{2.1}$$

where A is the cross-sectional area of the porous sample. This law is of great importance in science and engineering, but breaks down both in the small-scale limit (comparable with the pore size) and in the large-scale limit (km-scale). The permeability still remains a phenomenological constant, and although there are useful approximations to estimate a permeability, we are still lacking a full, generalized theory around the intermediate-scaled Darcy law.

2.2 Modeling the porous medium

In order to investigate the behavior of a porous media one can generally pick one of two options: Either you accurately recreate a sample of a real porous media, or you model the pore-scale behavior to find system-scale properties. The first can be done by using scanning techniques as micro-CT scans, but generally takes a while and cannot deal with

upscaling the sample. In this work we are going to model a 2D-porous media as a network with nodes and links, as illustrated in Figure 2.1.

Figure 2.1: Illustartion of the core idea of a pore network model. The left image represents a realistic 2D porous media with the solid material colored in black and the pore space in white. The right image represents a pore network model of our small sample, capturing the average flow properties of the real sample.

Such models are called Pore Network Models, and has been used extensively for several decades, such as the famous work by Lenomand et al. [13], and in more recent works as [14]. These models are coarse grained models of a porous media, sacrificing details on the pore scale for the benefit of upscaling the system. The pipes in the system have a randomly distributed radius to mimic the disorder in the system, enabling a wider range of possible geometries. According to [15], there are existing methods for creating a 3D Pore-Network model of scanned porous medias, however, we choose to study 2D-models for simplicity.

These models are not flawless, and offers less microscopic details than a full fluid dynamics solver, like a Lattice-Boltzmann method or any CFD-type solver. However, they have been used to recreate the qualitative behavior of flows through porous media, as proved in [13] where they demonstrated the network model could reproduce the 3 main phases observed in two-phase flows in porous media with *one* simulator, instead of using more specialized simulators for each of the phenomena, which is explained in Section 2.4.

2.2.1 Fluid flow in the links

When adopting a pore network model, one must define the relations between the pressures at the nodes and the flow rates in the throats, which drives the motion in the system. A prerequisite is the assumption that we are in the creeping laminar-flow regime, enabling us to ignore inertia-terms and turbulent effects. We follow the derivation in [9].

The governing equation for a cylindrical tube flow – the Hagen-Poiseuille equation – can be derived analytically for a simple single-phase pipe flow by directly considering the Navier-Stokes equations, where it is assumed a Newtonian, incompressible fluid:

$$\frac{\partial \vec{u}}{\partial t} + (\vec{u} \cdot \nabla)\vec{u} = -\frac{\nabla p}{\rho} + \nu \nabla^2 \vec{u}$$

We assume that all flow is at a steady state, hence $\frac{\partial(...)}{\partial t} = \frac{\partial \vec{u}}{\partial z} = 0$, ignoring the developing

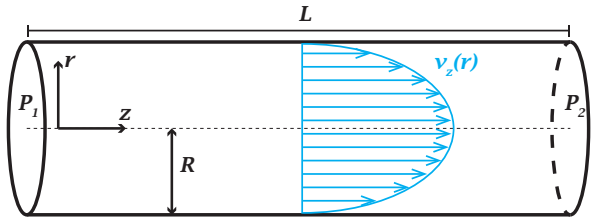

Figure 2.2: Illustrating a pressure-driven laminar tube flow, with the resulting velocity profile from equation (2.3).

region. We assume the flow is axisymmetric and is only in the z-direction of the tube, making $\frac{\partial(...)}{\partial\theta} = u_\theta = u_r = 0$. The Laplace-operator reduces to

$$\nabla^2 = \frac{1}{r}\frac{d}{dr}\left(r\frac{d}{dr}\right),$$

and hence the total momentum equation reduce to

$$\mu\frac{1}{r}\frac{d}{dr}\left(r\frac{d}{dr}u_z\right) = -\frac{dP}{dz} = -\frac{\Delta p}{L}, \tag{2.2}$$

where a uniform pressure gradient over a tube length L is assumed, making the pressure gradient $\nabla p = -\frac{P_2 - P_1}{L} = -\frac{\Delta p}{L}$. To solve this equation for the streamwise velocity, we try the solution

$$u_z(r) = -\frac{\Delta p}{4\mu L}r^2 + A\ln r + B,$$

and see by insertion that it satisfies the momentum equation. To avoid an infinite velocity at the centre of the tube, we must set $A = 0$, and we find B by setting the no-slip condition at the cylinder walls, i.e. $u_z(r = R) = 0$, making the final velocity profile

$$u_z(r) = \frac{\Delta p}{4\mu L}(R^2 - r^2). \tag{2.3}$$

The velocity profile is illustrated in figure 2.2 can be seen in the $\tau_c = 0$ case in figure 3.3. Integrating the velocity profile yields the flow rate in cylindrical tubes as

$$Q = \int_0^R u_z(r)2\pi r dr = \frac{\pi R^4}{8\mu L}(-\Delta p). \tag{2.4}$$

This is the Hagen-Poiseuille flow equation, proving a linear relationship between the pressure gradient and the flow rate in a tube flow, as well as a quadratic relationship between the flow rate and the tube radius. This law can be treated as the fluid analog of Ohm's law in electrical currents, where pressure gradient plays the role of a potential, flow rate the role of a current and the proportionality constant $\frac{\pi R^4}{8\mu L}$ the role of resistance.

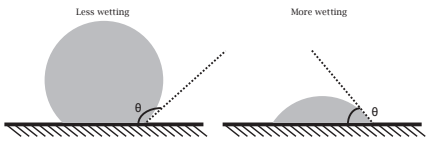

(a) Illustration on the concept of contact angle, dependent on the surface tensions in the interfaces. The left illustrates a less wetting phase with a high contact angle, while the right illustrates a more wetting phase which has a smaller contact angle.

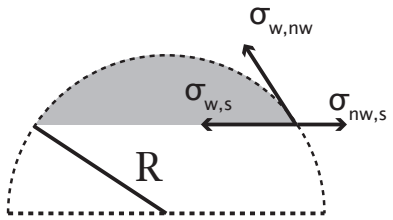

(b) Force balance in a two-phase-system, consisting of the 3 phases: a nonwetting phase (nw), a wetting phase (w) and the solid phase that makes up the porous media (s). The contact angle in the system is dependent on the properties of all 3 phases.

2.3 Capillary forces and meniscus dynamics

We're working on immiscible two-phase flows, meaning that we have some mechanism forcing the two fluid phases to stay separated from one another. These are capillary forces, which are the combination of adhesive and cohesive forces in an immiscible interface keeping molecules from the same fluid together. When new surfaces are created, some work is done to overcome these forces, expressed as $\delta W_{\min} = \sigma \delta A$, stating that the reversible work done on expanding or contracting the interface is proportional to the change in surface area between the two fluids. The proportionality constant, $\sigma > 0$, is an interface-specific constant, i.e. it is different in a water-air interface from a water-oil interface. This σ constant is what we define as *surface tension*.

In a porous media flow, we will have the case of 3 phases: 2 fluid phases and a solid phase. This creates the phenomena known as wetting, and is characterized by a contact angle in the interface of the 3 phases, as illustrated in 2.3a. A higher contact angle means the fluid is less wetting, hence we denote the 2 fluid phases as the wetting phase and nonwetting phase[1]. A force balance between the 3 surface tensions is formed, shown in figure 2.3b, and gives Young's law

$$\sigma_{s,w} = \sigma_{s,nw} + \sigma_{w,nw} \cos(\theta). \tag{2.5}$$

The effect of interfaces – called menisci – is a pressure difference between the fluid phases, which we will call the *capillary pressure* Δp_σ for this work. The pressure difference can be derived from (2.5), and gives the Young-Laplace law:

$$\Delta p_\sigma = \frac{2\sigma_{w,nw} \cos(\theta)}{R}. \tag{2.6}$$

An interface in a cylindrical tube will always be constrained by the tube radius R, which is assumed in the method. Hence, every link in the network will have its own interfacial pressures.

[1]This terminology might cause confusion, as we often call the limit cases $\theta \to 180^\circ$ (perfectly) non-wetting and $\theta \to 0^\circ$ (perfectly) wetting. Here we call the less wetting phase between the two *nonwetting*, and the opposite *wetting*.

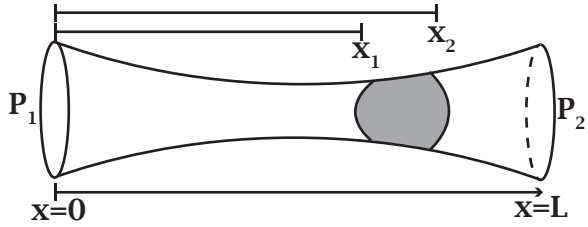

Figure 2.4: Illustration of the varying radius of the tube, to model the varying interfacial pressure. Since the meniscus at position x_2 has a larger radius than the one of x_1, we have a net force in the positive x-direction. The effect gives a competition between the pressure gradient and capillary pressure, giving rise to other phenomena as Haines jumps.

2.3.1 Capillary force in a tube with varying radius

If we look back on figure 2.1, assuming the links to have a completely uniform radius might be unrealistic for modeling a porous media. As the Young-Laplace law is dependent on the tube radius, the physical capillary force will vary with the meniscus positions in the tube, which has to be taken into account. Hence, we model the tubes as a slowly varying radius, assuming the flow equation for a straight tube 2.4 to still be valid for the model.

For instance, if we have a tube with one single blob of invading fluid, as illustrated in figure 2.4, there will be a net force on the blob. This force introduces a competition between the pressure gradient and the capillary force, which is an important competition when characterizing the large-scale phenomena, as we will see in chapter 2.4. This method of modeling the varying interfacial pressure has been used by [15], deriving the expression

$$\Delta p_\sigma(x) = \frac{2\sigma\cos(\theta)}{R}\left[1 - \cos\left(\frac{2\pi x}{L}\right)\right] \tag{2.7}$$

An interesting phenomena due to the varying tube radii is called Haines jumps, which are the jumps a bubble of nonwetting fluid when the net capillary force switches direction to go along the system pressure gradient. This will happen when the blob is just squeezed through the smallest tube radius, giving the blob of nonwetting phase an acceleration, making it ”jump” away from the throat. The effect may cause a larger scale avalanche effect in the system [16], and would be unphysical to exclude from our model.

2.4 The 3 Phases of Immiscible flow in Porous Media

2.4.1 The two key ratios

Two-phase flows in porous media is a complex system, making up very different characteristic patterns. We have two main competing mechanisms in the pressure gradient and the capillary pressure, and their relative strength is an important factor for determining which pattern the system will make after invasion. The work of Lenormand et al. in 1988 [13] proposed the phase diagram of which phase (or pattern) based on 2 dimensionless

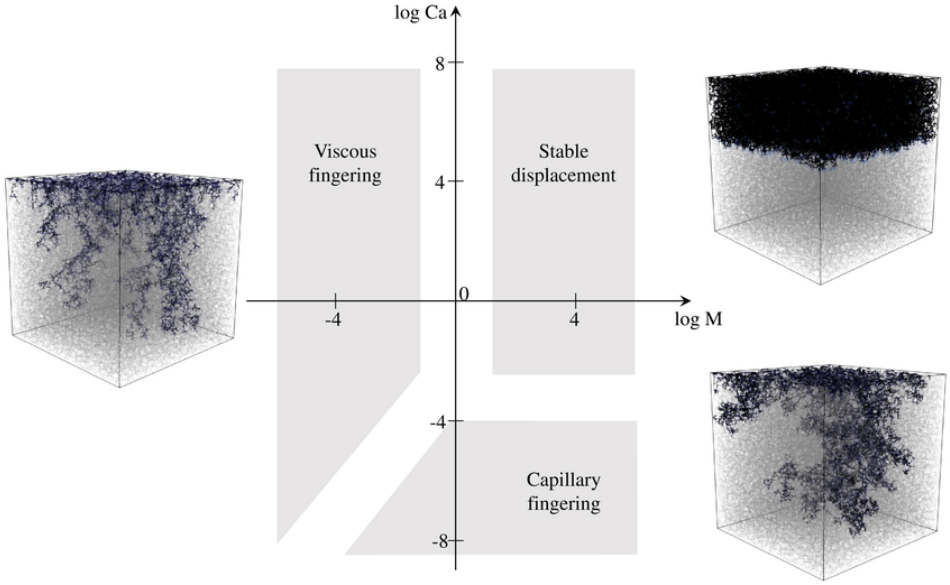

Figure 2.5: Phase diagram of immiscible two-phase flow patterns: viscous fingering for low viscosity ratios and high flow rates, stable displacement for high viscosity ratios and high flow rate, and capillary fingering in the capillary-dominated regime, i.e. at low flow rates. Image courtesy of [17].

numbers: the viscosity ratio M and the Capillary number Ca. The first is simply the ratio of the invading fluid viscosity, denoted with subscript i to the defending fluid viscosity with a subscript d:

$$M = \frac{\mu_i}{\mu_d} \tag{2.8}$$

The capillary number is defined as a ratio between the viscous forces and the capillary forces, which really is a local characteristic, since the viscous forces vary with velocity and capillary forces vary with the local tube radius. Still, we define the ratio as

$$Ca = \frac{Q\mu_d}{A\sigma\cos(\theta)}, \tag{2.9}$$

where Q is the total flow rate of the system, A is the cross sectional area of the porous medium, and σ and θ are defined in equation (2.6).

These resulting phase diagram is found in figure 2.5, showing the three main phases of two-phase Newtonian flows through porous media.

2.4.2 Fractal dimension

It appears that, for some systems, a certain self-similarity appears: The macroscopic shape is made up of smaller parts with the same shape. This phenomena is seen in nature, like in a cauliflower, a tree, river networks and coastlines, but also in complex nonlinear systems like clouds and flow patterns in porous media. The self-similar shapes are analysed by the

theory of fractals, based on the classic book by Feder, where the fractal dimension is a key concept for analyzing the self-similar patterns quantitatively [18]. We are used to the notion that a dimension is only an integer – the euclidean dimension D_E is 1, 2 or 3. If we now cover an euclidean object (i.e. a line, plane or cube) of length L with boxes with side length δ, and count the number of boxes N, we end up with the relation

$$N(\delta) = \left(\frac{L}{\delta}\right)^{D_E} \tag{2.10}$$

Hence, to cover a plane of length L with boxes of length $\delta = L/5$ takes 25 boxes, making its dimension 2. In these self-similar patterns, however, this same technique of box-counting will give a non-integer value, $D \neq D_E$. This noninteger dimension is what we call the fractal dimension, and measure how close a certain pattern is to a euclidean dimension – a fractal dimension of 1.8 would span most of a plane, while a fractal dimension of 1.2 would be closer to a line. This measure is useful for characterizing the differences between the 3 main phases in porous media flows.

2.4.3 Charaterizing the 3 phases

Each phase has its own underlying physical mechanisms, and can be associated with a statistical model reproducing these mechanisms, being active research topics themselves [2]. Here we are especially interested in characterizing these phases measuring macroscopic quantities like their non-wetting saturations at breakthrough, as well as their fractal dimensions.

Viscous fingering:

This phenomena is characterized by its thin, directed fingers, making the saturation of the invading fluid quite low, compared to the other phases. The viscous fingers have a fractal dimension $D \simeq 1.5$, and is much lower than for the other phases. The physical mechanism can be reproduced by the so-called directed percolation model, which has some very interesting critical behavior when adjusting the porosity in the sample, exhibiting a non-temperature driven second order phase transition [4].

Capillary fingering:

When we have much thicker diffusive fingers, we call it capillary fingering, happening at much lower capillary numbers (hence capillary forces are stronger) than for viscous fingering. An interesting aspect of the capillary fingers is the tendency to create trapping regions, which are islands of defending fluid trapped around some of the invading fluid. This phase is characterized by a non-wetting saturation close to the viscous fingering, but a higher fractal dimension, around $D = 1.8$. It exhibits similarities with dielectric breakdowns, modeled by Diffusion-Limited Aggregation. However, a recent study shows this physical modeling to miss some of the interesting ganglia dynamics happening in capillary fingering flows [19].

Stable displacement:

Stable displacement often occurs with water displacing air, and is therefore the most familiar phenomena, where the fluid makes a stable front with almost full saturation. The

[2] Actually, the Fields medal this year (2022) was awarded to Hugo Duminil-Copin for his contributions in phase transitions, having published several works on percolation theory, so the field is still attracting attention.

front makes a high fractal dimension, often close to 2. The phenomena is driven by an Anti-Diffusion-Limited Aggregation, which is another limit-case of the dielectrical breakdown model[13].

2.5 Simulation choices

Some choices has to be made in order to implement a full pore network model to simulate these two-phase flows. This section describes some of the more important choices that was made, implemented in all the results of the simulator.

Although the simulator may output flow fields, pressure fields, and various control values for each timestep, the most efficient way to analyse the behaviors is via images. Some resulting images can be seen later in the text, for instance in figure 2.8, and a scaled-up version is useful for illustrating some choices, as seen in figure 2.6

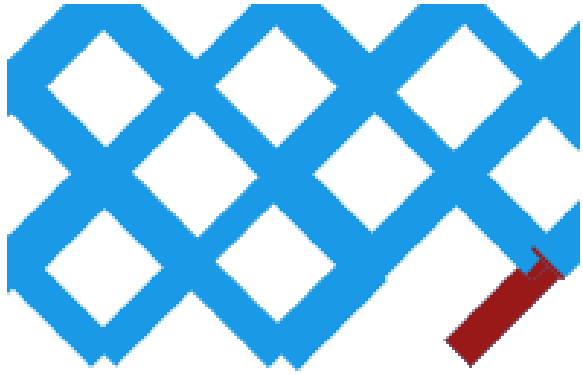

Figure 2.6: A zoom-in on an output image in the very first timestep, located at the inlet row. We can see that the radii are different in every link, but not by much, following a uniform distribution $r_i \sim \mathcal{U}(0.05, 0.25)$. We see the invading (nonwetting) fluid colored in red and the defending (wetting) in blue. The one inlet in the figure will always be completely filled with the invading fluid, and for simplicity "kill", or "switch off" the neighboring link to the inlet.

2.5.1 Tilted grid

The underlying geometry is a regular square lattice, tilted by 45 degrees. Every node is then connected to 4 links, which we define as SE, SW, NW, NE after the cardinal directions. The geometry of the underlying grid should not affect the results of the simulations when the grid becomes large, and it would be possible to change this geometry and compare it to another. The volume of the nodes is chosen to be 0, seen only as a mixing chamber, so all the fluid lies in the links. The disorder of the system is modeled only in the radius of the links, which are drawn from a chosen distribution, chosen to be uniform in this work. If a link radius is drawn to be less than 0, the link is simply switched off, and no fluid may pass through it.

2.5.2 Boundary conditions

The boundary conditions is set to be periodic along the y-axis (the left and right side of the output images) on and closed on the inlets and outlets, with the option of also closing all boundaries in order to make the simulation more related to experiments.

2.5.3 Imposing flow rate

To make the system actually move, there needs to be a driving force – an overall pressure gradient. This can either be chosen to be a constant pressure gradient, making the flow rate vary with time, or a constant flow rate, varying the inlet pressures with time. There are no immediate advantage of picking either, and both have their applications and can be done experimentally; we choose to set a constant flow rate, making the numerical solver calculate the inlet pressures. This choice is also done to easier compare the simulator to later experiments.

When imposing constant flow rate, every other link in the inlet row will be ”killed”, i.e. switched to inactive, while the remaining inlet links will be fully filled with the inlet fluid – seen in figure 2.6. This was a choice we made to ensure there are no bubbles present in the inlets, making the equation for inlet pressure the same for all time steps. The number of open inlets can be adjusted, and has been set to 1/10 of the total inlets for all simulations except the ones in Section 3.5.

The numerical solver for both the pressure and flow fields is discussed in chapter 3.3, as it is more related to the nonlinear rheologies. The method outputs the flow rate of every link in the system, and is iterated until a certain *stopping criterion.* This criterion is reached when we have a whole path of invading fluid all the way from an inlet to an outlet, where all the links in the path must be at least 90% filled with the invading fluid.

2.5.4 Bubble formation

After solving the flow equations for one time step, we know how much fluid goes in and how much goes out of one node, into the 4 links. However, a choice has to be made when there are two fluid phases going out of one node into several links: How much of each fluid? Following the example of [15], we choose to distribute the fluids democratically, meaning the ratio of fluid 1 to fluid 2 going into the node is the same as in all outgoing links. An example of this democratic distribution is illustrated in figure 2.7 A-D, and is the mechanism for generating more interfaces.

Now that we know the ratio of fluid 1 to fluid 2 going into the link, another choice must be made: Either, fluid 1 goes first, or fluid 2 will go first. It would not be quite right to set either to always go first, so this is done by setting fluid 1 to go first every even time step, and fluid 2 to go first every odd time step of the simulation.

2.5.5 Merging rules

When using the democratic distribution rules we generate more and more bubbles each time the two fluid phases meet in a node. However, it is not physical to have a link with a lot of bubbles, as they tend to merge when they are sufficiently close to one another.

However, how should the merging mechanisms be? Here, we use the same idea as [15], where the merging rules was discussed in detail, testing 3 different rules. The conclusion was to set an upper limit for number of bubbles in a link – the choice we made was maximum 3 bubbles – and then merge the two closest bubbles so that the centre of mass was conserved, as illustrated in figure 2.7 E. Also, there was an additional rule that a bubble in contact with a node will not move away from the node. To do so, the other bubble will merge into the bubble connected to the node, which [15] found to be the most physically sound modeling of the bubble merging rules.

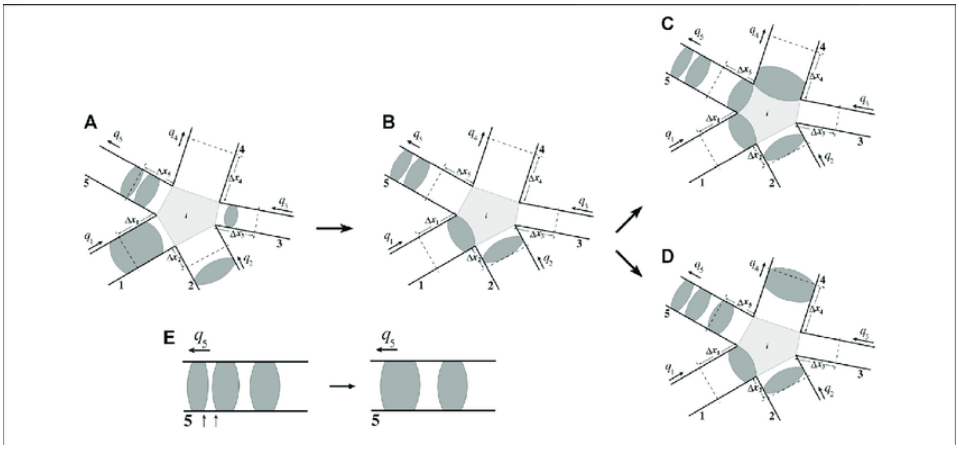

Figure 2.7: Illustrations of the algorithms handling the movement of bubbles in the simulator. The initial state is shown in A, along with its calculated displacements Δx_i from solving the flow field. In B, the fluid is transported into the node, seen as a mixing chamber. From the node, the fluid is distributed democratically: all fluid transported out of the link has the same ratio of grey to white fluid. Every even time step, the grey fluid goes first, shown as case C, and every odd step the white fluid goes first, as in D. Finally, we apply the merging rule in every link that has too many interfaces, as shown in E. Image courtesy of [15].

2.6 Simulating the Newtonian phases

The main goal of this chapter of Newtonian two-phase flows in porous media is to recreate the 3 characteristic phenomena with the numerical method, to demonstrate that it handles the realistic and relevant ranges of the two key ratios discussed in section 2.4.1.

The time-evolution of a viscous fingering pattern is shown in figure 2.8, showing a more compact region near the inlets, then spreading out into thinner fingers, spreading a bit out.

A capillary fingering displacement and a stable displacement is shown at breakthrough in figure 2.9a and 2.9b. Their characteristic traits – saturation and fractal dimension – are summarized in table 2.1, where their different characteristics become clear.

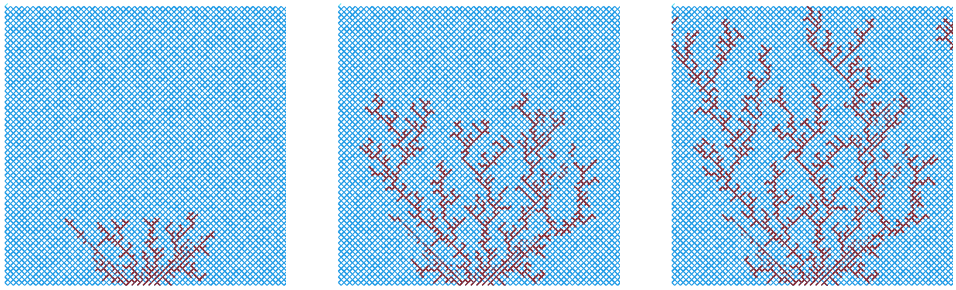

Figure 2.8: Time evolution of a viscous fingering flow, chosen timesteps are after 2000, 10000 and the breakthrough step at 15203 simulation steps for a grid of 50x50 nodes. The capillary number for the simulation was 10^{-2}, and a viscosity ratio of 10^{-3}, which is right on the edge of the viscous phase in the phase diagram.

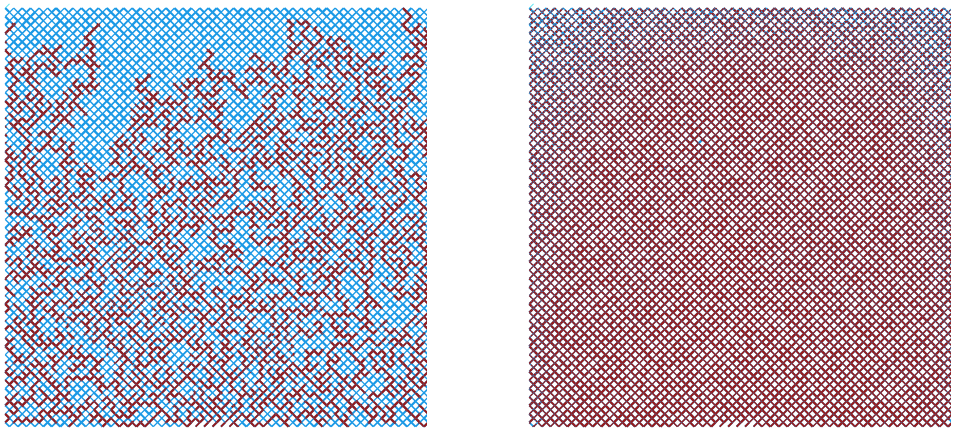

(a) **(b)**

Figure 2.9: (a) A simulation of capillary fingering, characterized by its many trapped clusters of defending fluid. The simulation was done with a grid of 50x50 nodes, and had an equal viscosity ratio and $Ca \approx 10^{-4}$. (b) Simulation of a stable displacement on the same grid as (a). Here, the viscosity ratio was $M = 100$, and the capillary number $Ca = 1.44$.

Figure	Phenomena	Saturation S	Fractal dimension D
2.8	Viscous fingering	0.22	1.79
2.9a	Capillary fingering	0.52	1.98
2.9b	Stable displacement	0.95	1.99

Table 2.1: Summary of the saturations and the fractal dimensions of the 3 characteristic patterns in a Newtonian two-phase flow.

3

Yield Stress Fluids

3.1 The Rheology of a yield stress fluid

As mentioned in the introduction, Bingham saw necessary to departure from classical hydrodynamics, as their work showed that some materials are something in between a solid and a liquid. They present a non-linear viscosity, resisting stresses up to a certain critical stress – the yield stress – where it starts to flow. Stresses below this yield stress will just stretch the material, but not deform it.

In [8] we find the rheological constitutive equation relating the stresses s, deformations ε and flows $\dot{\gamma}$:

$$\begin{cases} s - \tau_c = 2\eta_{pl}\dot{\gamma} & \text{for } |s| > \tau_c \\ s = 2\mu\epsilon & \text{for } |s| < \tau_c \end{cases} \tag{3.1}$$

where τ_c is the yield stress, illustrated in 3.1 and η_{pl} is the plastic viscosity.

3.2 Pipe flow of the Bingham fluid

The flow rate in a cylindrical tube flow can also be derived analytically for a yield stress fluid from considering the stress tensor directly. Here we will follow the derivation from [8], starting off with the rheological equation for the Bingham fluid (3.1), with $|s| \geq \tau_c$. As in the derivation for Newtonian pressure tube flow (2.2.1), it is assumed that the only velocity profile is $\vec{u} = u_z(r)$, i.e. that $u_\theta = u_r = 0$. Hence, the only component of the flow tensor left is

$$\dot{\gamma} = \frac{du_z}{dr} = u_z'(r). \tag{3.2}$$

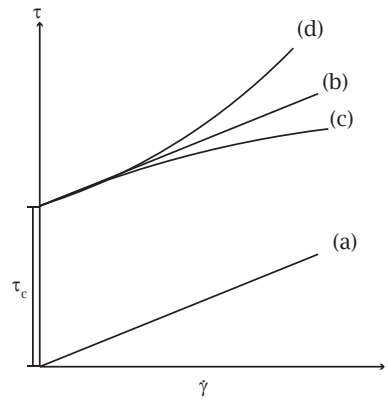

Figure 3.1: Different approximations to the rheological constitutive equation – the relation between shear stress, τ, and rate of strain $\dot{\gamma}$ – of a real fluid. The most ideal is the Newtonian approximation (a), followed by the Bingham body in (b) which has a yield stress τ_c. (c) and (d) are examples of index fluids, having a yield stress and a power-law; (c) is shear thinning and (d) is shear thickening.

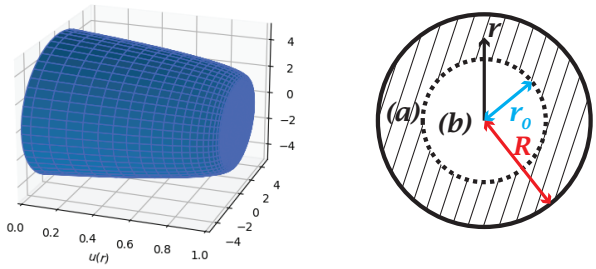

Figure 3.2: The Bingham fluid will have a region in the centre remaining unyielded, making two regions in the velocity profile: one flowing and one behaving as a solid, named region (a) and (b) respectively, as seen in the right illustration.

By inserting in (3.1) we find all the elements in the stress tensor

$$\begin{cases} s_{zz} = s_{\theta\theta} = s_{rr} = -p \\ s_{r\theta} = s_{z\theta} = 0 \\ s_{zr} = s_{rz} = -\tau_c + \eta_{pl} u_z'(r) \end{cases} \tag{3.3}$$

Due to the yield stress effect, there will be two regions to consider in this tube flow: one inner cylinder from the centre with a radius r_0 which moves like a solid plug with constant velocity u_0, and we have one outer region between the plug and the tube wall $r \in [r_0, R]$ where the material will flow, illustrated in 3.2. Starting with the flowing region, (3.3) is inserted into the stress equation in the z-direction for cylindrical coordinates:

$$\frac{\partial s_{rz}}{\partial r} + \frac{1}{r}\frac{\partial s_{\theta z}}{\partial \theta} + \frac{\partial s_{zz}}{\partial z} + \frac{s_{rz}}{r} = 0, \tag{3.4}$$

yielding the equation analogous to the Newtonian case (2.2):

$$\frac{dp}{dz} = \eta_{pl}\left(f'' + \frac{f'}{r}\right) - \frac{\tau_c}{r} \tag{3.5}$$

Once again, the pressure is assumed uniform over the tube with length L, hence

$$\frac{dp}{dz} = -\frac{\Delta p}{L}.$$

Inserting in (3.5) and integrating over r yields

$$-\frac{\Delta p}{L}\frac{r^2}{2} = \eta_{pl} r f' - \tau_c r + C_1 \tag{3.6}$$

To find the integration constant C_1, we must have a look at $r = r_0$ where the flow starts. Here we know the stress is exactly the same as the yield stress $s_{rz} = \tau_c$, and combined with (3.3) we see that $f'(r = r_0) = 0$. Hence from (3.6) we have

$$\tau_c = \frac{\Delta p}{L}\frac{r_0}{2} + \frac{C_1}{r_0} \tag{3.7}$$

and since the pressure forces, acting on the area πr_0^2 must be equal to the yield stress on the rim of the solid inner cylinder, we have that

$$\frac{\Delta p}{L}\pi r_0^2 = \tau_c \cdot 2\pi r_0, \tag{3.8}$$

and hence $C_1 = 0$ from combining (3.8) with (3.7). Integrating (3.6) once more over r yields

$$-\frac{\Delta p}{L}\frac{r^2}{4} = \eta_{pl} r f - \tau_c r + C_2 \tag{3.9}$$

and this other integration constant C_2 can be found by the kinematic boundary condition $u_z(r = R) = 0$, i.e. that the flow is 0 along the tube wall

$$C_2 = \tau_c R - \frac{\Delta p R^2}{4L} \tag{3.10}$$

By reinserting $u_z(r)$ for f, we get the final expression for the velocity in the flowing region

$$u_z(r) = \frac{\Delta p}{4L\eta_{pl}}(R^2 - r^2) - \frac{\tau_c}{\eta_{pl}}(R - r) \tag{3.11}$$

Setting the no-slip condition between the solid plug and the flowing region yields the plug velocity

$$u_0 = u_z(r = r_0) = \frac{\Delta p}{4L\eta_{pl}}(R^2 - r_0^2) - \frac{\tau_c}{\eta_{pl}}(R - r_0) \tag{3.12}$$

We see that this velocity profile for the Bingham fluid yields the same as the Newtonian case seen in equation (2.3) when $\tau_c \longrightarrow 0^+$ and $\eta_{pl} = \mu$. In total, the velocity profile of a Bingham body in a cylindrical tube is seen in Figure 3.3.

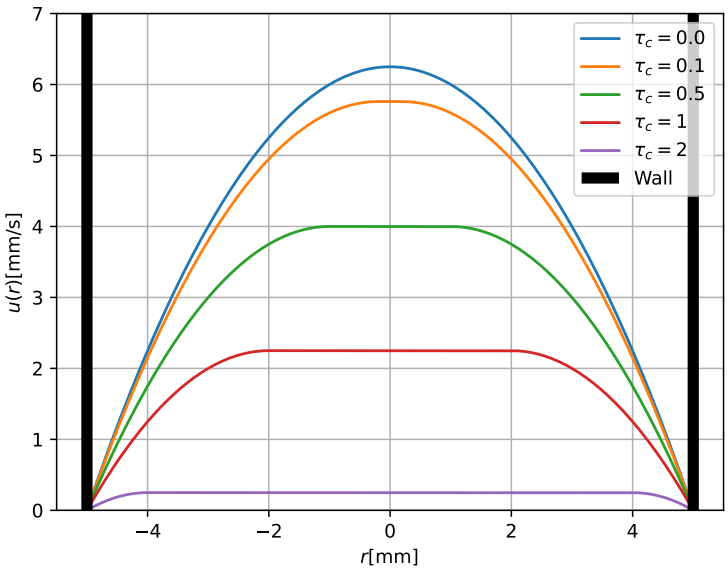

Figure 3.3: Plots of the velocity profile $u_z(r)$ for varying values of τ_c, as found in equations (3.11) and (3.12). The plot for $\tau_c = 0$ gives us the familiar Poiseuille velocity profile, derived in chapter 2.2.1.

Finally, integrating the velocity profile across the whole tube yields the total volumetric flow rate

$$\begin{aligned} Q = 2\pi \int urdr = 2\pi \left[\int_0^{r_0} u_0 r dr + \int_{r_0}^{R} u_z(r) r dr \right] \\ = \frac{2\pi}{\eta_{pl}} \left[\frac{R(R^2 - r_0^2)\Delta p}{8L} - R\tau_c(R - r_0) + \frac{R^2 \Delta p}{4L} \left(\frac{R^2 - r_0^2}{2} \right) \right. \\ \left. - \frac{\Delta p}{4L} \left(\frac{R^4 - r_0^4}{4} \right) - \tau_c \left(R \frac{R^2 - r_0^2}{2} - \frac{R^3 - r_0^3}{3} \right) \right] \end{aligned} \tag{3.13}$$

Finally, by using (3.8), one finds the relation between yield stress and solid plug size

$$r_0 = \frac{2L\tau_c}{\Delta p}, \tag{3.14}$$

combining with (3.13) we have derived the Buckingham-Reiner equation:

$$Q = \Delta p \frac{\pi R^4}{8\eta_{pl} L} \left[1 - \frac{4}{3} \frac{2L\tau_c}{R\Delta p} + \frac{1}{3} \left(\frac{2L\tau_c}{R\Delta p} \right)^4 \right] \tag{3.15}$$

As expected, the Buckingham-Reiner equation yields the Hagen-Poiseuille flow equation (2.2.1) for $\tau_c = 0$.

3.2.1 Unyielding stresses

The flow rate relation was found assuming there was a sufficiently large stress so the fluid would flow – however, as we see in the $\tau_c = 2$ case in figure 3.3, high yield stresses will give very low velocities, and at some point there will be no flow. Hence, we must impose another condition on the flow rate in a single tube, namely that

$$Q = 0 \quad \textit{if} \quad \Delta p < p_\tau = \frac{2\tau_c L}{R}, \tag{3.16}$$

where the critical threshold pressure p_τ is exactly where the fluid will start flowing. The effect is a nonlinear relation between pressure gradient and flow rate, shown in figure 3.4. We see that the 4th power term in equation (3.15) falls off very rapidly, and can generally be ignored for lower yield stresses.

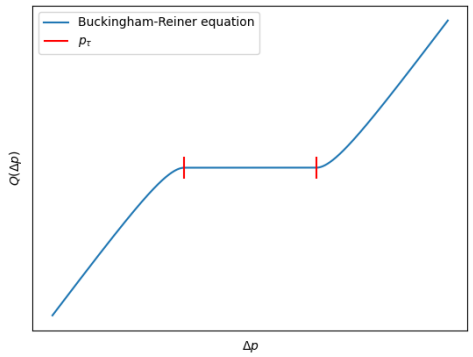

Figure 3.4: The derived relation between pressure and flow rate for a single tube flow of Bingham fluid. The critical threshold pressure p_τ is also shown in the relation.

3.2.2 Flow of two fluid phases in a tube

When there are two phases of fluid in one tube, there will be interfaces with their corresponding interfacial pressures P_σ. In addition, since the flow-pressure relations are dependent on the fluid viscosities, the amount of fluid in a tube matters. If the tube of volume V is filled with a volume of V_N Newtonian fluid phase and $V - V_N = V_B$ Bingham fluid phase, the flow rate becomes

$$\begin{cases} Q = \frac{\pi R^4}{8\eta_{pl} L} x \left[1 - \frac{4}{3}\frac{2L\tau_c}{Rx}\right] \frac{V_B}{V} + \frac{\pi R^4}{8\mu L}\frac{V_N}{V} x - \frac{\tau_c L}{R} & \text{if } x > \frac{\tau_c L}{R} \\ 0 \quad \text{else} \end{cases} \tag{3.17}$$

Here, we defined $x = |\Delta p - P_\sigma|$ and we compute P_σ as the effective capillary pressure summed over all interfaces, $P_\sigma = \sum_i p_\sigma(x_i)$ from equation (2.7).

3.3 Agumented Lagrangian Method

In the framework of the pore network model, one is interested in finding, for every node i and every link (ij), the pressure P_i and the flow rate q_{ij}, where the indices i and j run over the ensemble of nodes of the network. Being the relation between the pressure and the flow rate (3.17) non-linear, we need to solve a system of *coupled* and *non-linear* equations efficiently. This constitutes a computational challenge, and although one could use the pore-scale Lattice-Boltzmann method, as in [20], or using the numerical method of [21], larger systems has remained a challenge to simulate. Recently, Talon and Hansen presented their Agumented Lagrangian Method, which was used for simulating another non-Newtonian fluid – a bi-viscous fluid [22]. Our numerical method is based on this work, and is capable of handling other non-linear rheologies, like an index fluid (illustrated in figure 3.1, case (c) and (d)).

The method is done in 3 steps, where the idea is to include 2 virtual parameters: one acting as a virtual current field, and one as a virtual pressure field. These parameters acts as Lagrangian multipliers, and comes with the constraints that they should converge into their physical twins, namely the fields $\{q_{ij}\}$ and $\{P_i\}$ respectively, making additive constrictions. The Kirchhoff condition expresses mass conservation in the bulk of the system, analogous to the well known condition in electrical systems:

$$\sum q_{ij} \quad \forall \, \textit{Node} \tag{3.18}$$

Adding the equations for tube flow, one can solve the system in 3 core steps which will be repeated until the system converges. We must therefore make it clear that we define two types of timesteps: Every time the 3 core steps has been repeated, we have done an *inner* timestep, and once this lagrangian method has reached convergence, all meniscus positions is updated, which is an *outer* timestep. Note that the inner steps has nothing to do with the actual time, while the outer steps are related to the physical time.

The 3 core steps follow the structure of [22]:

Step 1:

The first step in the method is solving for the pressure field $\{P\}$ at the nodes and virtual currents $\{j\}$ in the links. The step is expressed in a system of equations, solving for the pressures, based on the flow equation that the pressures in the nodes and current in the links are related by some mobility constant, expressed in

$$A\{P\} = B,$$

where the A-matrix expresses the mobility constants. In the bulk of the system, these are set to a global common constant, α, and the pressures and currents will eventually relax into their physical values. In the bulk, A is defined as

$$\begin{cases} A_{ii} = \sum_{ii \in n.n} \frac{1}{\alpha} \\ A_{ij} = \frac{-1}{\alpha} \quad \textit{if} \quad ij \in n.n. \end{cases} \tag{3.19}$$

The notation n.n. stands for nearest neighbor, meaning that A will generally be $\frac{4}{\alpha}$ in the diagonal, $\frac{-1}{\alpha}$ in the 4 corresponding links, and 0 everywhere else. The exception is in the

inlets and outlets. For the inlets, we set actual physical mobility, σ_{ij}, found as the first factor of equation (3.15) as $\sigma_{ij} = \frac{8\nu_{pl}L}{\pi R_{ij}}$ between link i and j. Hence the inlets will have the values

$$\begin{cases} A_{ii} = \frac{1}{\sigma_{ij}} \\ A_{ij} = \frac{-1}{\sigma_{ij}} \quad if \quad ij \in n.n \end{cases} \tag{3.20}$$

The outlet links are simply set to 1, as these are the only place we do not have mass conservation. The matrix does not change during the simulation, and is therefore found in the initialization.

The vector B is found by calculating the corresponding currents, where the first and last elements correspond to the inlets and outlets, respectively:

$$B^{(n)} = \begin{pmatrix} Q_{in} \\ ... \\ \sum_{k \in n.n.,1} \mu_{1k}^{(n)} - \alpha q_{1k}^{(n)} \\ ... \\ \sum_{k \in n.n.,i} \mu_{ik}^{(n)} - \alpha q_{ik}^{(n)} \\ ... \\ P_{out} \end{pmatrix} \tag{3.21}$$

After solving for the physical pressures, we update the the virtual flow field $\{j\}$. For the very first outer timestep, one will have to guess an initial value blindly, while for the other timesteps, one just use the values from the previous outer timestep. We use the equation

$$j^{(n+1)} = \frac{1}{\alpha}\Big(\Delta P^{(n)} + \mu^{(n)} + \alpha q^{n}\Big),$$

for all positions.

Step 2

Now we would like to find the currents q, and do so via the step

$$f(q^{(n+1)}) + \alpha q^{(n+1)} = \mu^{(n)} + \alpha j^{(n+1)},$$

where the function f is the equation for the total physical pressure drop. In the case of a link of Bingham fluid with one Newtonian blob of length x_m, we get that:

$$f(q) = \frac{8\mu_N \cdot L}{\pi R^4} \cdot x_m q + \frac{8\eta_{pl} \cdot L}{\pi R^4} \cdot (L - x_m)q + \frac{\tau L}{R} + P_\sigma, \text{if } |\mu + \alpha j - P_\sigma| > \frac{\tau_c L}{R}$$

The P_σ is the effective capillary pressure in the interfaces, and is calculated from equation (2.7).

Step 3

We update the multiplier-parameter μ by the formula:

$$\mu^{(n+1)} = \mu^{(n)} + \alpha(j^{(n+1)} - q^{(n+1)})$$

This was the method for doing *one* inner timestep.

3.3.1 Convergence and deciding the physical timesteps

As described in [22], the algorithm is iterated until the fields have relaxed into a value – the convergence criterion is set to a relative change of less than 10^{-7}. After the system has converged, one can update all the positions of all the menisci according to their velocity, decided from the flow field. However, one has to decide the physical timestep to simulate. It could be set into a constant, but this would restrict the simulator to a certain range of velocities, as we couldn't trust the high-velocity simulations, and the low-velocity simulations would take too much time. Therefore, for each *outer* timestep, we identify the fastest tube velocity $\max(v)$, and set the physical timestep as

$$t = \frac{1}{10} \frac{L}{\max(v)} \tag{3.22}$$

3.4 Immobilization effects in a defending Bingham fluid

Since the yield stress effect prevents the Bingham fluid from flowing, the most interesting results will occur when the Bingham phase is the defending fluid – after all, the invading fluid will have an imposed velocity, so this has to flow. Hence, all the simulations is done as Newtonian fluid displacing a Bingham fluid. For a defending Bingham phase, there will be a certain path that will minimize the total yield stress that must be overcome – the path of least resistance. We find this path using the Dijkstra algorithm, as done in [14] as well.

In order to qualitatively analyze these kinds of flow patterns, two new coloring elements are included in the simulations: Light blue is the immobilized Bingham fluid, and the path of least resistance is visualized by coloring the edges of the tubes red. In this way one can qualitatively separate the different phases and phenomena for the yield stress effects.

The magnitude of the yield stresses and the related threshold pressure that must be overcome offers another dimensionless parameter along with the viscosity ratio and the capillary number. We define the yield number, N_τ, as

$$N_\tau = \frac{\tau_c \cdot R}{\sigma}, \tag{3.23}$$

which expresses the ratio of yield stress pressure to capillary pressure. To define this number for a disordered system, we use the mean value of the tube radius distribution for R in (3.23).

The results of 16 simulations with varying yield numbers and capillary numbers are shown in figure 3.5 and show qualitatively what happens for an increasing value of τ_c.

An interesting phenomena in the high yield stress regime ($N_\tau = 0.1$) is the fact that an increasing capillary number gives us a higher saturation, which is the opposite of what is happening in the Newtonian case, where the fingers tend to become more directed for higher capillary numbers. The capillary forces simply cannot overcome the yield stress effects, and we see some very thin, narrow fingers for the lowest capillary number, and thicker fingers in for higher Ca.

Another interesting behavior with the immobilization is the leftmost image of figure 3.6. We see a certain tree-like structure, resembling a lightning pattern. A very similar

pattern occured in [23], where minimal paths in flux lines were studied and a ground state energy defined.

Also, there are some interesting things that can be studied in depth, like the shapes and sizes of the clusters of immobilized fluid. For instance, the simulations with N_τ in figure 3.5 show patterns with well-defined immobilized clusters, and their evolution and distribution could be an interesting phenomena to study further.

3.5 Power law behavior

An effect caused by the yield stress at low flow rates is the opening and closing of channels; at very low flow rates, only one channel will be open the whole way from inlet to outlet, and for high flow rates all channels are open. This effect, seen in Figure 3.6 is causing a deviation from the Darcy Law, which predicts a $\beta = 1$ in

$$Q \propto (\Delta P - P_{th})^\beta.$$

For a yield stress fluid the effect has been investigated earlier by [21] and [14], proving that we expect a power-law behavior with $\beta \approx 2$ in this low-Q-regime. The power-law behavior is analogous to a work by Roux and Herrmann in networks of nonlinear electrical resistors with a voltage-to-current relation similar to the pressure-to-flow rate relation in figure 3.4 [24].

To find the value for β, one has to actually find an appropriate value for the minimal system threshold pressure P_{th}. If there is only one open channel – namely the path of least resistance – the calculation is simply summing the yield stress pressures, τ_{ij} over the path. For a system of paths, however, one must compute the limit

$$P_{th} = \lim_{Q \to 0} \frac{1}{Q} \sum_{l \in \mathcal{L}} \tau_{ij}\, q_{ij}, \tag{3.24}$$

which yields the threshold pressure of the system in the stable state.

Another way to find this threshold pressure is to assume a power-law behavior for the first few decades, and find the pressure that minimizes the least squares deviation from the power-law. In general, this error will have a parabolic shape, making it easy to find the best fit for the pressure. The subroutine to find the best pressure fit is:

```
  for beta
    find power law for beta
    for P_th
      find square error for the dataset
    pick the P_th value that minimizes square error

  find the lowest minimized square error, and
  pick these beta and P_th values

```

Such a routine demands an initial guess in both fitting parameters, which is easy, as we know the threshold pressure from the easiest path, named P_{in} as well as $\beta \approx 2$. The standard deviation of the best power-law fit is seen in figure 3.7a.

With the chosen value for P_{th}, one can fit a power law to the first two decades, yielding a final value for β, with the final power law seen in Figure 3.8.

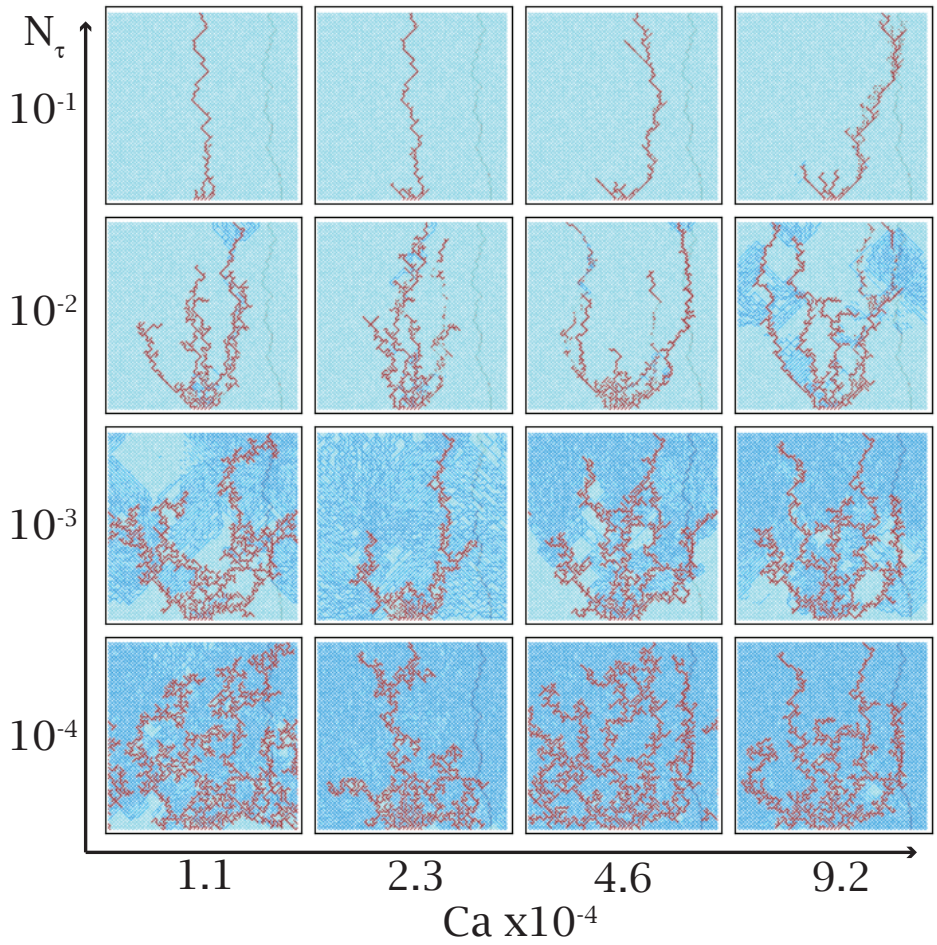

Figure 3.5: Simulation results for varying levels of imposed flow rate and yield stress, as shown with the dimensionless parameters Ca and N_τ. All simulations was done with 50x50 nodes and 5 inlets, until breakthrough. The invading fluid is colored in red, mobilized defending fluid in dark blue and immobilized defending fluid in light blue. A faint path can be seen in the figures, which is the calculated path of least resistance.

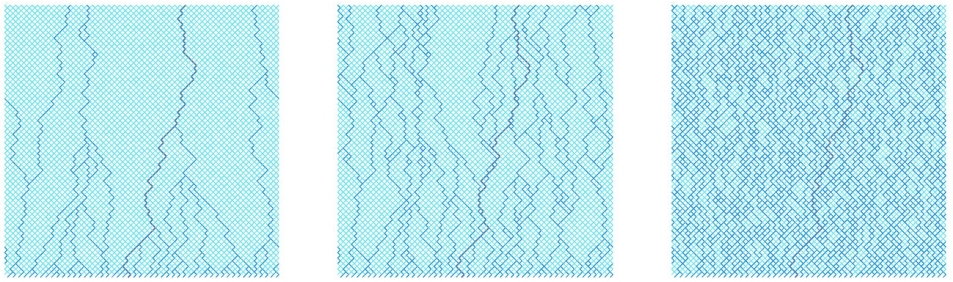

Figure 3.6: Increasing the imposed flow rate opens more channels and creates more available paths for the fluid to flow. Going from left to right, the imposed flow rate is 10^{-5}, $16 \cdot 10^{-5}$ and finally $256 \cdot 10^{-5}$, all simulations done on a 50x50 grid.

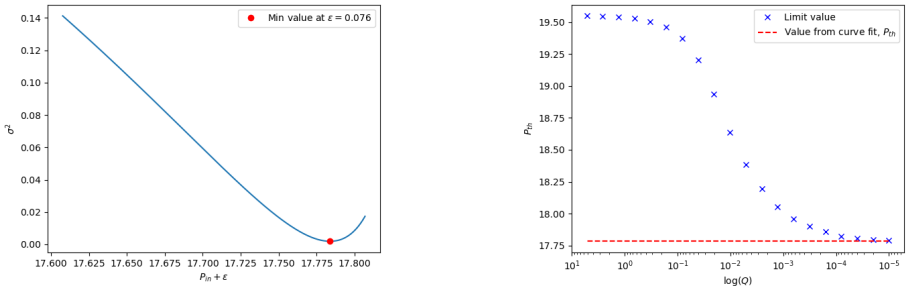

(a) **(b)**

Figure 3.7: (a) Least square error for the two first decades in Figure 3.8, giving the best fit for β and P_{th}. ε is the difference from the single-channel threshold pressure. (b) Plot of the equation (3.24), which will converge to the threshold pressure when $Q \longrightarrow 0$. The threshold pressure from the curve fit is also plotted, making a good match with the lowest flow rate $Q = 10^{-5}$ with only a negligible difference.

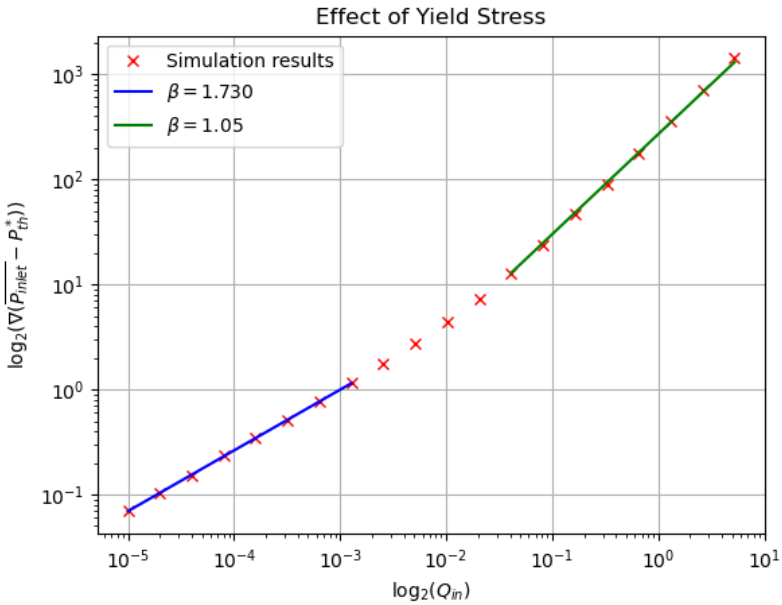

Figure 3.8: Power law fit to the single-phase simulations, exhibiting two regimes in the relation between pressure gradient and flow rate in the pore network model. Note that the transition happens somewhere between $\log_2(Q_{in}) = -1$ and -2.

4

Conclusion and further work

In this thesis a network model has been implemented along with an Agumented Lagrangian Method to handle the nonlinear rheology of a Bingham fluid. The main focus of the work was to verify the modeling choices and to explore the effects of the yield stress in a two-phase flow, laying a solid foundation to explore its properties further. The first benchmark for the model was to recreate the 3 well-known Newtonian phases, which was done by comparing their non-wetting saturations and fractal dimensions at the breakthrough of the invading fluid. There are two key ratios deciding the resulting pattern, namely the viscosity ratio and the ratio of viscous forces to capillary forces present in the system links. In total this makes up a phase diagram.

The modeling of the links was particularly important, as it would be too naïve to simply assume a regular Hagen-Poiseuille flow in the tubes – capillary forces vary in the link, and is therefore modeled by a varying link radius. The rules for handling bubbles is also an important feature of the simulator and is based on the recent findings of [15].

The real challenge was to do the same type of simulations for a yield stress fluid, as this makes a non-linear rheology: These are fluids that will not flow unless there are exposed of a stress that exceeds their yield stress. These are studied by using the simplest case: the Bingham fluid, which has a yield stress, and then a linear relation between imposed stress and strain rate. The Buckingham-Reiner equation is derived for the Bingham fluid in a tube flow, describing the relationship between pressure and flow rate. Implementing these non-linear relations in the code is a computational challenge, and is solved by a recently developed method from [22]. This method decouples the system of equations and make use of the Kirchhoff condition expressing mass conservation, and introduce two virtual fields with each their constrictions, enabling us to solve the system equations with an iterative scheme.

The results of the simulations with a Bingham rheology qualitatively showed the effect of the yield stress, since the flow pattern was more directed for higher yield stresses. An heuristic explanation is that for high yield stress only a few channels are open, so the invading fluid displaces the defending one only in few directed paths from the inlet to the outlet, even for low capillary numbers, for which, in the fully Newtonian case, wider and

more spread patterns are expected.

A quantitative result was given by the power law relation between the flow rate applied and the pressure drop measured. The exponent found was associated with an increasing number of open channels, each of which having an increasing flow rate. The steady-state behavior of a single-phase flow was then investigated, in order to isolate the yield stress effect, making the expected power law of $Q \propto (\Delta P - \Delta P_{th})^{\beta}$, with a $\beta = 1.73$ in our simulations.

In further work, a lot can be done, as these systems still remain unexplored. Exploring various ranges of the input parameters and characterizing their behaviors would be a step towards finding a full phase diagram for Bingham fluids as well. The immobilization seems to form clusters, and it would be interesting to characterize these clusters along with their distributions and their shapes. The mobilized channels form a certain tree-like structure, resembling the concept of a ground state energy in flux lines – something that would be possible to define in these systems as well. Finally, expanding the simulations to index fluids would make it possible to study the two-phase flow of a more realistic fluid rheology, adding a shear thinning or -thickening effect to the fluid. Furthermore, running some two-phase flow experiments on yield stress fluids would make a good comparison with the simulation results, and will be looked into in a later work.

I intend to go further in this direction in my master thesis, following this specialization project.

Part II

Statistical Properties of a Single-Phase Bingham Fluid in Porous Media

(Master's thesis)

5

Introduction

In the project thesis – part I – we did the preliminaries for studying yield stress fluids in porous media, building up a pore-network model along with a numerical scheme that was used for solving the flow equations for the whole two-phase flow system. Considerable effort was put into handling the menisci[1] of our system with realistic yet not too time-demanding algorithms, and modeling choices like hourglass-shaped tubes and well thought-through rules for handling the menisci were picked to allow for net capillary forces and phenomena like Haines jumps in the simulations. The importance of the capillary forces were made obvious in chapter 2, and displacement patterns of two-phase flow is certainly a more technologically and industrially interesting field than single-phase flows. Still the title of this thesis states that we are mainly interested in studying the case of one single phase, and the question of why has to be answered.

We present 4 main reasons for why we consider it relevant to focus on single-phase Bingham fluids in this Master's thesis, even though we have the tools for studying two-phase flows.

5.1 The complexity in analyzing a two-phase flow with yield stress effects

In chapter 2 we introduced the force competition between viscous fingering (the Saffman-Taylor instability) and capillary forces in a two-phase flow and its resulting three phases in the phase diagram. In chapter 3 we introduced the concept of the yield stress fluid and the Bingham model, along with a numerical solver to analyze these yield stress fluids in a pore-network model. Although the simulator can handle two-phase flows with yield stress fluids, Figure 3.5 showed us the complexity encountered when introducing another

[1] Actually, when presenting this work for the Porous Media community on the Interpore 2023 conference, one of the comments we got pointed out was the error of not putting *more effort* by using a more complex, velocity dependent equation for the pressure in the menisci. Our claim is that the Young-Laplace equation is sufficient for these models, as we can assume quasistatic conditions as long as the imposed flow rate isn't too high.

parameter into this force competition. As physicists, we are used to reducing a systems complexity until we are able to *properly* understand what is going on, all this *before* we increase the complexity to make the system more realistic. For instance, calculating air resistance is almost never relevant in an introductory course in mechanical physics, as they aren't relevant to the forces at play in the concepts at hand; it will be ignored until you take more advanced courses when you are ready for the complexity or when you need to engineer and can accept a more "black-box"-approach. Doing single-phase flow is the same, in that we reduce the complexity to study the isolated effect of yield stress, as the litterature in the field is lacking.

The ultimate goal of this project is to move one step closer to finding the total phase diagram, and in order to do so, we need to properly understand and quantify how the yield stress effect will work in a pore-network simulation. We argue that looking at the single-phase case will be the best way to find its net effect, before introducing the two other forces that come into play, as we will briefly do in chapter 8.

5.2 Relation to Newtonian two-phase flows

This argument follows from the work of Sinha and Hansen in 2012 [25], pointing out the similarity.

A generalized Darcy equation for a *Newtonian two-phase flow* is stated as

$$Q = -C \cdot \frac{A}{L} \frac{K(S_{nw})}{\mu_{eff}(S_{nw})} \cdot sgn(\Delta P) \cdot \begin{cases} |\Delta P| - \Delta P_c, & \textit{if } |\Delta P| > \Delta P_c \\ 0, & \textit{else} \end{cases} \tag{5.1}$$

with the effective viscosity simply being the saturation-weighted average

$$\mu_{eff}(S_{nw}) = \mu_{nw} S_{nw} + \mu_w \cdot (1 - S_{nw})$$

Here we see that the whole formulation is highly dependent on the ΔP_c, which is the system's pressure barrier due to capillary forces – a relation discussed in the project thesis in chapter 2, governed by the equation for interfacial pressure (2.7).

Their idea is to see this ΔP_c as analogous to the one we find in single-phase Bingham flows, following the same underlying structure as the electrical network in [24] namely that only a certain number of channels are open – ΔP_c is stronger than the local pressure gradient in the remaining closed channels. If we call the number of open channels $\mathscr{N}$, we can make the argument that increasing the pressure by some amount dP will increase the number of open channels $d\mathscr{N} \propto dP$; then when new channels open up, it effects the total system conductivity Σ. Thus we may conclude that there is some relation $d\mathscr{N} \propto dP \propto d\Sigma$. This applies until we reach a limit where $d\mathscr{N} = 0$, where all capillary pressure thresholds have been overcome, and the system will behave linearly, described by the Darcy equation.

One of the main interests in the project thesis was the transition discussed in section 3.5. It turns out Newtonian two-phase flows have the same power-law relation as seen with Bingham fluids: the flow rate is scaling quadratically with pressure in the transition region, and then linearly for sufficiently high pressures, resembling a fully yielded Bingham fluid system, as was stated in the equation

$$Q \propto (\Delta P - P_{th})^{\beta}, \tag{5.2}$$

with 3 regimes for the value of β:

$$\beta = \begin{cases} 1, & \textit{Single tube regime} \\ 2, & \textit{Transition regime} \\ 1, & \textit{Fully open regime} \end{cases} \tag{5.3}$$

The power-law relation is shown in Figure 5.1, implies that a Newtonian two-phase flow and a Bingham single-phase flow will have the same effective rheology, so finding statistical properties of this Bingham fluid system expands to two-phase flows, and also more generally in certain network systems, as for instance the mentioned electrical networks in [24].

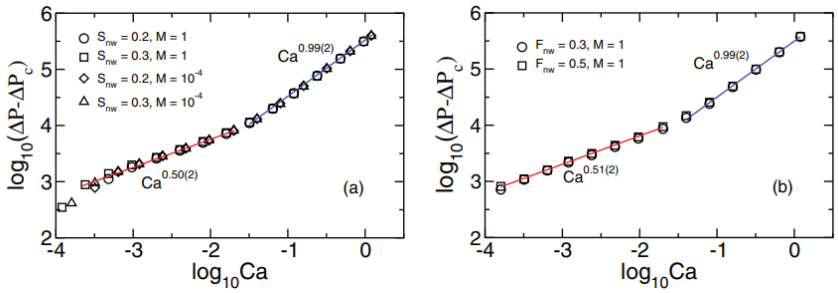

Figure 5.1: The resulting power-law relations from Sinha and Hansen in [25]. We see clearly two regimes, where the low-capillary number regime yields a $\beta = 2$ in 5.2, similar to the transitional regime in the single-phase Bingham system. Image courtesy of Sinha and Hansen [25].

Foam flows in porous media is one of the types of Newtonian two-phase flows where this analogy to single-phase Bingham flows are relevant. This is very much an active research question too, and the creation and impact of foam in porous media flows has recently been studied by Lanza et al. [26]. This work indicates a transition between viscous fingering and foam creation in a very similar simulation technique as the one we introduce in part I.[2]

There is however one important point to make at the end of this argument, namely that the analogy breaks down in the infinite-scale limit. When system size $L \to \infty$, we will always have a path throughout the system without any capillary-induced threshold pressure, and the flow behaves as Newtonian again [27].

5.3 Relation to statistical physics

Mentioned in the outlook of the project thesis, there is a ubiquitous relation to the world of statistical physics in these pore-network simulations, where critical phenomena, Kardar-

[2] In fact, the simulation code is practically the same, but with an imposed pressure gradient instead of an imposed flow rate.

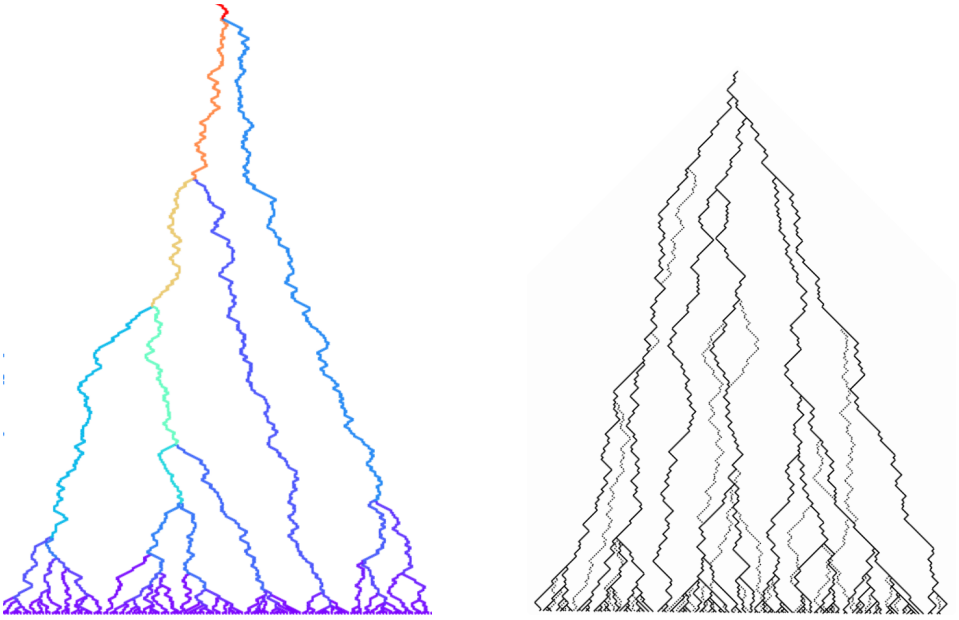

Figure 5.2: Comparison between the simulated flow field (left) and the work of Drossel and Kardar in [23] (right) showing minimal paths in 2D (solid) and the energy barriers between them (dotted).

Parisi-Zhang[3] theory on growth patterns, and complex networks[4] are hot topics that could be linked up to single-phase Bingham flows.

The most immediate relation comes from a work by Drossel and Kardar [23] on flux lines in high T_c type-II superconductors – a system descirbed by the problem of the Directed Polymer in Random Media (DPRM). They propose a model, and then explore the statistical physics of the pattern that emerges, as seen in Figure 6.1 where their work is compared to one of our simulations, exhibiting a striking similarity. This similarity comes from the underlying complex structure that describes them both, and their patterns show up generally when finding the best energy paths [28], dynamic scaling of a growing interface [28] as well as describing common everyday-phenomena like river networks [29] and which way you should pick for going to Rome[5].

In general, statistics of the system are interesting when looking to upscale our systems, and there is currently a great effort into creating quasi-thermodynamic theories for porous media flows [5] and toolkits from statistical physics are certainly needed in order to solve the scaling issues we still do not fully understand.

[3] Giorgio Parisi won 1/2 of the Nobel Prize in physics in 2021 for his work on "for the discovery of the interplay of disorder and fluctuations in physical systems from atomic to planetary scales", where this equation plays a central role. We also refer to other works by Kardar [23] and Zhang [28].

[4] One of the biggest names in network science is surely professor Albert-László Barabási, who in fact started his career in the field of porous media flows. His theories on complex networks has become relevant in several popular fields, like neural networks, neuroscience, computer networks and human dynamics.

[5] As the saying goes: "all roads lead to Rome" – but which one to pick isn't always that obvious!

5.4 The utility of single-phase yield stress fluids

Even though the preliminaries in the project thesis allow us to study Yield stress fluids in two-phase flows, it should be stated that there is utility and relevance in studying single-phase flows too. For instance, an experimental method for extracting the pore size distribution by injecting yield stress fluids was developed and tested in 2014 by de Castro [30], and extracting porous properties by non-Newtonian fluids has attracted recent interest due to its simplicity and non-destructive properties [31].

This technique uses a capillary bundle model, where the porous structure is modeled as a bundle of non-interacting long thin tubes. As we have seen over and over, tubes filled with yield stress fluids will have a pressure barrier until they start to flow, so when slowly increasing the imposed forces, one may extract the distribution of radii by observing when each tube will yield. The technique will give a rough estimate of the porous structure – de Castro showed a comparison to another porosometry technique, showing their proposed yield-stress method certainly could be improved; these method might benefit by modeling the interactions between these capillary bundles – a network model – instead.

Another example of the utility of studying these single-phase yield stress fluids is the relation to granular flows. The effective rheology of a granular debris flow can be modeled as a non-Newtonian fluid by the Herschel-Bulkley rheology (a more generalized model than the Bingham rheology, see case (c) and (d) in Figure 3.1) with a non-negligible yield stress [32].

In all, properly studying and understanding yield stress fluids in porous media is of value in itself, and is an important step towards achieving what could be called the holy grail of this work: defining the full phase diagram of yield stress fluids in porous media, analogous to the one introduced for two phase flows in chapter 2 (Figure 2.5).

6

Defining and exploring the ground state

In order to understand the transition from an immobilized to a fully mobilized system, we need to understand what happens when the imposed forces in the system goes to zero. In general, there are two ways to impose the forces on the fluid: by applying a constant pressure difference or by applying a constant flow rate. The case of an imposed pressure difference on these systems were studied numerically by [33] and [21], who were able to predict the minimal threshold pressure of the system. In general we define the total pressure barrier due to yield stress in a path $\mathcal{P}$ through links $ij \in \mathcal{P}$ as

$$\Delta P_c = \sum_{ij \in \mathcal{P}} \frac{2\tau_c L}{r_{ij}} = \sum_{ij \in \mathcal{P}} \tau_{ij}. \tag{6.1}$$

For any imposed pressure below the quantity ΔP_c all the fluid will remain immobilized.

In our case, we are interested in exploring the case of an *imposed flow rate*, achieved by imposing the flow rate in every inlet link. This will create what we define as a system state, $\mathcal{S}$, where the pressure barrier due to yield stress will be defined similarly as (6.1): the sum of yield pressures in all yielded links. The number of yielded links will depend on the flow rate we impose, and similar to the work by [23] we know there will be some state minimizing this exact quantity. Hence, we define the ground state $\mathcal{GS}$ as the state minimizing

$$\mathcal{GS} := \min(\sum_{ij \in \mathcal{S}} \tau_{ij}). \tag{6.2}$$

As these local yield stresses only depend on the local link radius $\tau_{ij} \propto r_{ij}^{-1}$, we aim to, without doing any simulations at all, define the disordered landscape of minimum yield pressure sums from each inlet to each other point in our network. Finding the easiest path through such a disordered landscape is a problem one may encounter in various situations, and is usually solved with using a variation of Dijkstra's algorithm.

6.1 Finding the Ground State

This section is based on a work by Talon et al. "Geometry of Optimal Path Hierarchies" [34].

Finding the easiest path through a disordered network is a problem of great interest in many fields. For instance, it is a key concept when using the GPS-based navigation services that most people rely on in a day-to-day basis. There are an endless amount of ways to do navigate from one point on the map to another, and perhaps none of the ways are immediately optimal when taking speed limits and traffic into account. In order to do this, we break the road network down to a network of nodes where we have crossroads and links where we have the connecting roads. To find the optimal path, one must have data on the time it takes to travel through each link in the network – a value we denote t. Then, we find the total time from the start point $\vec{r_i}$ to the finishing point $\vec{r_f}$ via the path $\mathcal{P}$ as

$$T_1 = \min \sum_{\vec{r} \in \mathcal{P}} t_{i,j(i)}, \tag{6.3}$$

doing the minimization over all possible paths, making T_1 the minimal sum of $t_{i,j(i)}$ through the network. The notation $t_{i,j(i)}$ is used to clarify that the j-values are the addresses of all links connected to node i.

To find our desired optimal state, we use the notion of a *pathscape*, which is the field containing information of the minimized paths from each node i in the system to the outlets, defined as

$$V_i \to V_i = \min_{j(i)} \left(t_{i,j(i)} + V_{j(i)} \right). \tag{6.4}$$

To find T_1 from the pathscape, we simply start from our position r_i, and for each node we pick the link that minimizes the value of $V_{i,j(i)}$, iterating through towards the finishing position r_f.

In our specific case, we wish to pick the optimal path from every single inlet, to any outlet, i.e. one specific $\vec{r_i}$ to a set of outlets $\{\vec{r_o}\}$. Our parameter to minimize is the local link yield pressures $t \to \tau_{ij}$ effectively working as the inverse link radius $1/r_{ij}$. In our network, every node is connected to 4 links where 2 are directed along the imposed flow rate – along the x-direction; we use the information that the optimal path must be directed [35] to speed up the algorithm – both when identifying the *pathscape* and when iterating through it. A pseudocode of the ground state algorithm is:

```
SET V = 0 at all nodes i and j
FOR i in system length L:
    FOR j in system width W:
        FIND V in the two directed neighbors
        SET V[i][j(i)] = min(V+t) of the two neighbors

SET GS = 0 at all links i and j(i)
FOR all inlet links:
    FOR i in system length L:
        FIND V in the two directed neighbors
        FIND the connecting node with min(V+t)
        SET GS[i][j(i)] += Qin at the link connecting

```

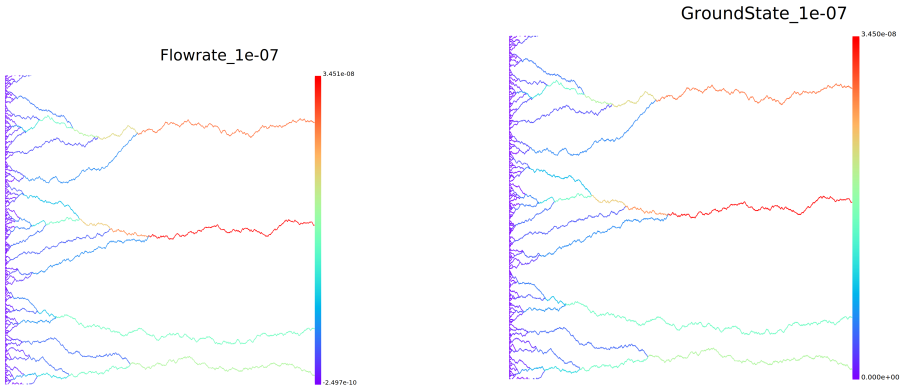

Figure 6.1: Comparison between a simulation with a relatively low imposed flow rate (set to $Q = 10^{-7}$) along with the predicted ground state, able to predict the exact same flow rates in the links. The fluid is going left to right, and a constant flow rate is imposed in every inlet at the leftmost boundary.

This will then output the optimal flow field through our whole system, when only taking the yield pressures into consideration.

6.2 The Predicted Ground State

A comparison between the predicted ground state and the simulated system can be seen in Figure 6.1, where we see an almost perfect match between the two, producing exactly the same flow rates in the exact same tubes, with an error of less than 0.1% of the links, due to numerical errors playing a role when lowering the imposed flow rate sufficiently.

Being able to predict exactly how the system will behave for low flow rates without simulating anything is one of the main topics in this thesis, and enables us to find other properties of the single-phase Bingham flow by only knowing the radii of the pore-network.

6.2.1 Benchmarking: Revisiting Figure 3.7b

In the project thesis, we wanted to look at the Darcy relation for Bingham fluids, proposed by several others in the case of an imposed pressure (see for instance [21, 14]) as

$$Q \propto (\Delta P - \Delta P_c)^{\beta}.$$

We argued that in our case for an imposed flow rate, the ΔP_c had to be replaced by an effective threshold term P_{th}, found by the limit

$$P_{th} = \lim_{Q \to 0} \frac{1}{Q} \sum_{l \in \mathcal{L}} \tau_{ij}\, q_{ij}. \tag{6.5}$$

This threshold pressure is exactly what defines the ground state: it is defined such as we minimize this P_{th}, giving us the theoretical minimum. Thus the ground state enables us to predict this term in the Darcy equation just from knowing the radii in the network, and holds for any general network, as long as the conditions discussed in [28] are satisfied: there can be no self-intersections, and the polymer can only fluctuate in the transversal direction – thereby always staying directed. These conditions will apply in our case as long as the disorder is sufficiently large, but not too large: if the disorder is too small, we are left with something much more similar to a random walk process, and if the disorder is too large the path starts back-bending, hence losing the directedness [35].

Revisiting Figure 3.7b, we can see if this claim that we're able to predict the Darcy relation actually holds. The pressure associated to yielding pressures from (6.5) should converge down to the predicted value as $Q \to 0$, and should always be equal or higher than our predicted lowest value associated to the ground state; this will be our benchmark, and can be seen illustrated in Figure 6.2.

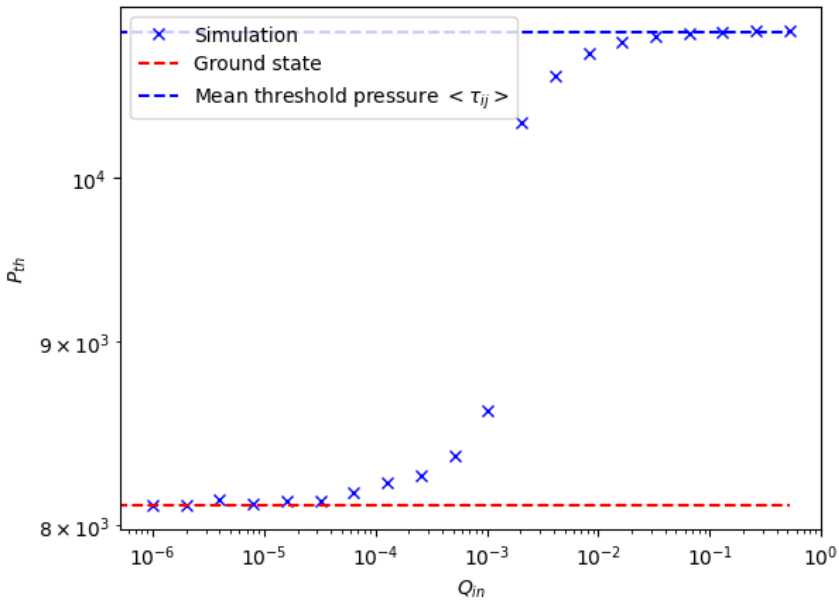

Figure 6.2: Simulation values of the yielding pressure for different flow rates (crosses) converging down to the threshold pressure when the flow rate goes to zero. Results are shown with the prediction from the ground state (dashed red line) and the average link yielding pressure $\langle \tau_{ij} \rangle$.

In addition, note that we are also able to predict the value of P_{th} as it flattens when the flow rate Q increases by one simple argument. When the flow rate increases sufficiently, the whole system will be yielded, and since P_{th} expresses the total pressure associated to yielding the fluid in each link, τ_{ij}, it will go towards the average link yielding pressure, $\langle \tau_{ij} \rangle$. This argument mostly serves as an additional sanity check in our analyses.

6.2.2 Scaling of branches in the ground state

As discussed in the introduction, the link to the problem of directed polymers in random media (DPRM) has been made clear. One property of the DPRM is the roughness – a measure of how much the polymer's end point will deviate (in its transversal direction) from its start point. The roughness is measured by:

$$\Delta y \propto L^{\zeta} \tag{6.6}$$

where the ζ_{DPRM} in a 2D directed polymer is known to be exactly $\zeta = 2/3$ [28, 35].

Now, when inspecting the system in ground state (right part of Figure 6.1) we notice that the paths will only merge, and that there is no backflow, as was some of the requirements for linking it to the DPRM theory. With the known result for the roughness exponent, we can expect the amount of branches n to drop off in a similar fashion, like

$$n(x) = n_i \cdot x^{-\nu}, \tag{6.7}$$

with n_i as the imposed amount of inlet branches. A comparison to simulations is shown in Figure 6.3, showing a clear power-law decay as expected.

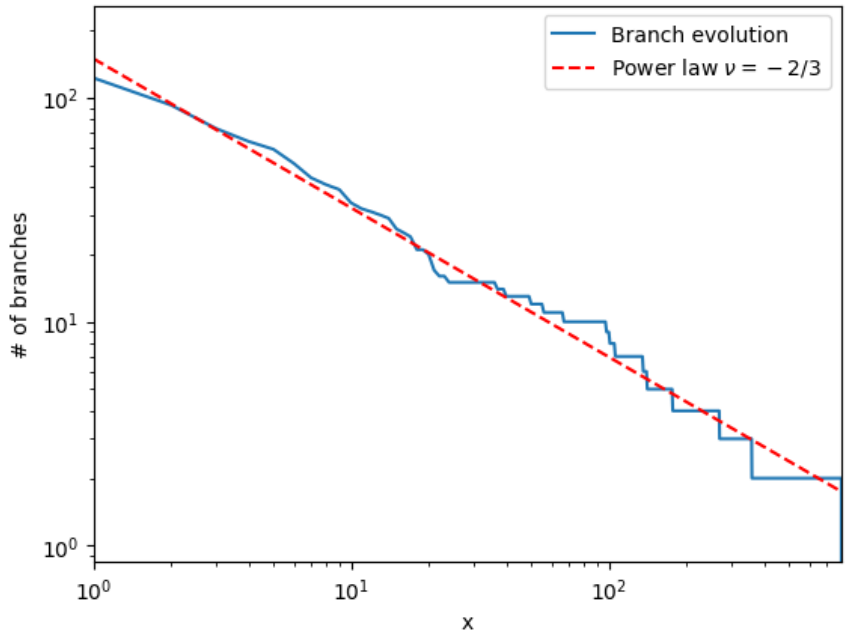

Figure 6.3: Evolution of the yielded branches of the network in Ground State. We set a fixed number of yielded links in the inlet row at $x = 0$, and know that the limit $x \to \infty$ will leave us with only one link.

6.3 Size of immobilized clusters

Another immediate property one may study is the characteristics of the clusters of immobilized fluids emerging in the system. These clusters were studied in the work of Chevalier and Talon [36] in a Lattice-Boltzmann method with an imposed pressure gradient, and showed a clear power-law relation for the two different types of disorder initialized in the system, where the clusters were distributed like

$$p(S) \propto S^{-\tau} \tag{6.8}$$

where τ[1]was found lie between 1.4 and 1.55 for the two compared initializations. In plain text, the probability p of finding a cluster of size S decays with a known rate, predicted by this power law.

In our case, we can measure without considering or fitting any other parameters like scaling of flow rate, and utilize one of the conditions we have from knowing this is a directed polymer problem: since we know that every flowing channel is *directed*, we have no back-flow, and the channels will only merge – it will never branch. Hence, we are able to find the cluster sizes quite easily by just considering the difference between two neighboring channels:

$$S_i = \int_0^L (y_i - y_{i-1})dx \tag{6.9}$$

When measuring the exponent, one choice has to be made, which is the bin sizes when making the histogram. We choose a logarithmically distributed bin, and get the power law exponent of $\tau = 1.4$, which is quite similar to the discussed case of an applied pressure as a boundary condition.

Related to this, finding the cluster length in the case of the directed polymer will be trivial, as we only need to find where two neighboring polymers merge, as shown in Figure 6.4. Once more we expect a power-law relation and define[2]

$$p(l) \propto l^{-\lambda}. \tag{6.10}$$

When measuring this length distribution in the same fashion as the size distributions, we find $\lambda = 1.6$, which deviates slightly from the values from [36], who measured a slightly higher exponent.

6.4 Triggering avalanches

This section is based on a work by Aragón et al. on "Avalanches in tip-driven interfaces in random media" [37].

When dealing with directed polymers in random media (DPRM), we take the optimal path, but what if we asked ourselves: how much would it change if we took a slightly less optimal path? Finding the second best or third best path is often just as interesting as the

[1]Note that here, τ refers to a power-law exponent, and not the yield stress, which will be called τ_c or τ_{ij}.

[2]Note that this exponent is called β in the original work by Chevalier and Talon, but is changed here to avoid confusion with the β defined in 5.2.

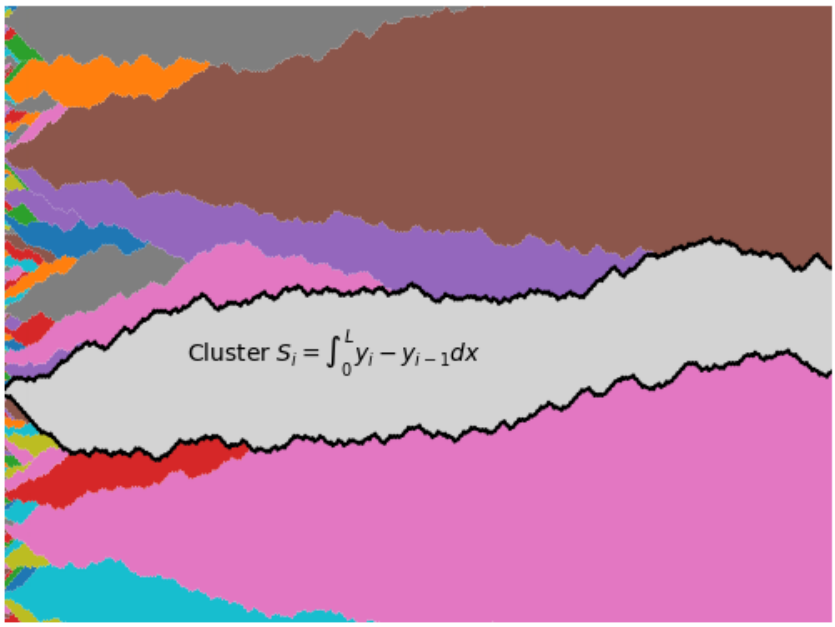

Figure 6.4: Illustration of the different clusters, characterized by their respective sizes and lengths, which we expect follow a power-law distribution.

optimal one, and modern GPS navigator systems usually display a few options instead of just the optimal one, as long as the differences are small. This idea can also be studied in these networks, where we are interested in answering how the DPRM would change when exposed to a weak potential.

The idea is to expose the whole network to a parabolic potential $U(x) = m(x - w)^2$, such that it will become biased towards the value w. For instance, if a DPRM of $\langle x \rangle = 150$ is exposed to a parabolic potential with $w = 160$ it might be beneficial to form a different polymer closer to $\langle x \rangle = 160$, depending on the strength of m and the characteristics of the network. The choice of m is set to be sufficiently weak that the strength of our potential $U(x)$ to be comparable to the average yield pressure τ_{ij} when $|x - w| \approx 100$. However, as long as we are in the weak-potential limit, the choice will be arbitrary.

We thus iterate through different values of w, and run the Dijkstra algorithm through the system, exposed to this potential. We repeat this with slowly increasing w, until the directed polymer changes to another. When a new polymer occurs, we can quantify the total area between the old DPRM and the new one; we call this area the size of the avalanche in the network, illustrated in Figure 6.6.

As long as these increments in w are small enough, these avalanches will only occur in one place along the polymer, which is what we want; here we can find its length and size, ranging from the smallest 2-link avalanches to the big ones making completely new polymers. These sizes are predicted to follow a power law relation with a predicted

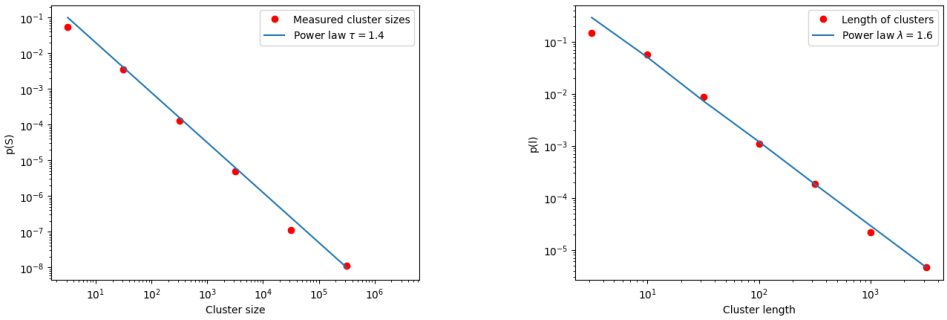

Figure 6.5: Measurement of the sizes and lengths of the immobilized clusters emerging in the ground state case. Both histograms used a log-spaced bin, with the largest cluster occupying 56% of the total area.

exponent[3]:

$$p(S) \propto S^{-\tau}; \quad \tau = 2 - \frac{1}{1+\zeta}, \tag{6.11}$$

with ζ as the roughness of the directed polymer, equal to 2/3. This leaves us with the predicted power-law exponent of $\tau = 1.4$.

Implementing the technique, we end up with the power-law as shown in Fig 6.7. We see the data better fits the exponent $\tau = 1.2$, which is somewhat surprising. Some factors playing in is the system size, only being WxL=400x1600 links, and the fact that we impose open boundary conditions on the sides $y = 0, y = W$. However, we have no proper explanation for this anomaly from the theoretical value.

[3] We use the exponent τ to indicate this is a cluster size exponent, but is not necessarily the same as in equation (6.8)

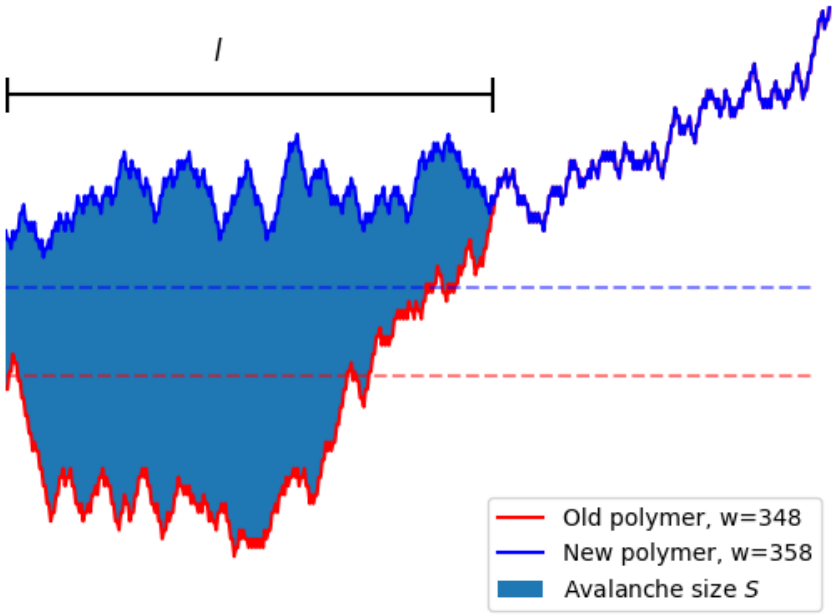

Figure 6.6: Example of an avalanche in the network, illustrating how we find the size and length of each cluster.

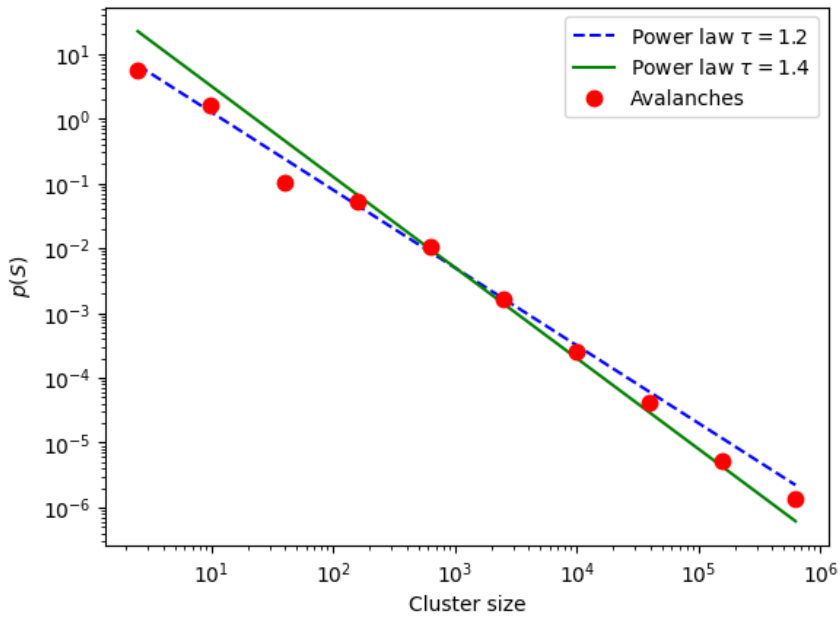

Figure 6.7: Resulting avalanches from imposing a total of 1000 different values for w iteratively from $w = 0$ to $w = W = 400$.

7

Characteristics of the transition

Having found some of the properties of the ground state, one may start looking at how these will behave as imposed flow rates increase. We have already seen the relation between pressure and flow rate, making a transition region characterized by the quadratic relationship $Q \propto (\Delta P - P_{th})^2$, and the yielding of new channels in the network, shown in Figure 7.1.

7.1 Immobilized clusters in higher flow rates

One of the most obvious features of the transition is the areas where we have immobilized fluids. These areas, or clusters, were studied in the ground state to follow the power-law in equation (6.8), and there are no other litterature on how these will behave when increasing imposed flow rate. Will, for instance, the power-law relation still hold for a certain range, and can we predict the size of the biggest cluster?

Finding these kinds of properties is of great interest, as it might serve as a clear distinction between different types of phenomena in porous media flows. For instance, it is an important feature when looking at the capillary fingering domain in a newtonian two-phase flow, where the defending fluid will form clusters. Measuring such clusters and its distributions may be a way of extracting information from the pore structure and flow properties, which would be our ultimate goal for studying these systems.

7.1.1 The Hoshen-Kopelman algorithm

In order to find the clusters for a system outside its ground state, we cannot use the same simple algorithm as in chapter 6.3, as this algorithm used the fact that we were dealing with directed polymers. In the case of a higher flow rate, the paths will split, so we simply need to use a more robust algorithm: The Hoshen-Kopelman algorithm. This algorithm is a variant of the union-find-algorithm, and is able to label the whole system in one sweep, making it an efficient way of labeling data clusters in general 2D or 3D systems [38]. A modified version of the algorithm is described with the pseudocode:

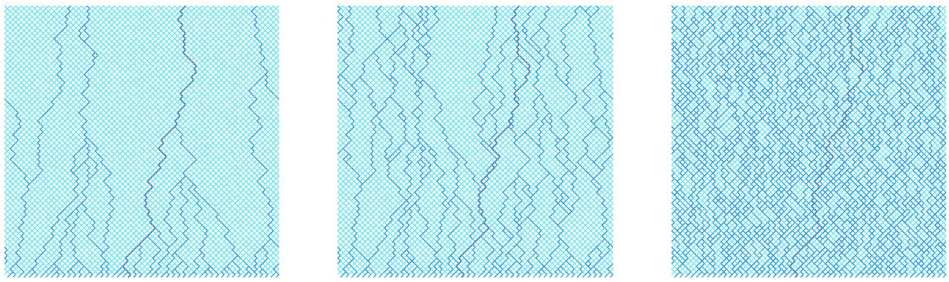

Figure 7.1: Repeating Figure 3.6 showing the transition we refer to in this chapter.

```
SET max_label = 1
FOR i in x_tot:
    FOR j in y_tot:
        SET left = grid[i][j-1]
        SET up = grid[i-1][j]
        IF grid[i][j] = 0 -> continue
        IF grid[i][j] != 0 -> switch:
            CASE 1: left = up != 0 -> SET grid[i][j]=left
            CASE 2: either left or up is 0, but the other is labeled ->
    SET grid[i][j]=max(left, up)
            CASE 3: left=up=0 -> grid[i][j] = max_label + 1; max_label +=
    1
            CASE 4: left and up are labeled, but with different labels ->
    UNION(left, up)

```

In plain text, the algorithm will iterate through every grid-point and evaluate the two neighbors to the left and above current position. We will then have 4 possible cases, and output a grid where all the connected clusters will have the same label, making it easy to find the shape and total size of each cluster.

We illustrate with an example system, shown in Figure 7.2, which could be part of a result from our network. This example system will have the matrix-form:

$$\begin{pmatrix} -1 & 0 & 0 & -1 & 0 \\ -1 & -1 & -1 & -1 & -1 \\ -1 & 0 & 0 & -1 & -1 \\ 0 & -1 & -1 & 0 & -1 \\ -1 & -1 & 0 & 0 & -1 \end{pmatrix}$$

If we now only include nearest neighbors (i.e. only the sites above, left, right and below are counted as neighbors) we see there will be 2 clusters in the system of size 12 and 4.

For each element, one checks the label to the left and the label above our current value, with the possible cases described in the flowchart. Hence, iterating from the top left corner

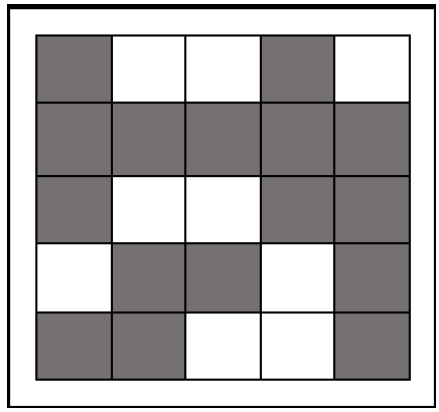

Figure 7.2: Example system for the Hoshen-Kopelman algorithm. The two colors represent fluid A (grey) or B (white), and our task is to find the sizes of the grey clusters.

in our matrix example yields

$$\begin{pmatrix} 1 & 0 & 0 & -1 & 0 \\ 1 & 1 & -1 & -1 & -1 \\ 1 & 0 & 0 & -1 & -1 \\ 0 & 3 & -1 & 0 & -1 \\ 2 & \textcircled{-1} & 0 & 0 & -1 \end{pmatrix}$$

And we see that we get a conflict at the circled position [2, 5] in the matrix, which will set the union between 2 and 3. After completing the algorithm, we are left with the labeled matrix:

$$\begin{pmatrix} 1 & 0 & 0 & 1 & 0 \\ 1 & 1 & 1 & 1 & 1 \\ 1 & 0 & 0 & 1 & 1 \\ 0 & 2 & 2 & 0 & 1 \\ 2 & 2 & 0 & 0 & 1 \end{pmatrix}$$

7.1.2 Adjustment to fit our particular network structure

A problem occurs when implementing the Hoshen-Kopelman algorithm in a tilted grid, namely the fact that some diagonal links should count as the same cluster, as seen in Figure 7.3.

The basic algorithm must therefore be adjusted in order to count this cluster as one 7-sized cluster instead of one 3-sized and four 1-sized ones. The problem is that this rule only applies for links parallel to the one we are evaluating, hence, for the northeastern links we must check the diagonal to the upper left, while for a southeastern link we must check the lower left diagonal. We add the following pseudocode when looping through the grid:

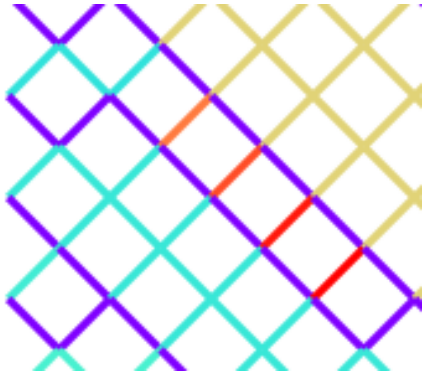

$$\begin{pmatrix} 0 & 0 & 0 & 4 & 4 & 4 & 4 & 4 \\ 1 & 1 & 1 & 0 & 4 & 4 & 4 & 4 \\ 0 & 0 & 0 & 5 & 0 & 4 & 4 & 4 \\ 2 & 2 & 2 & 0 & 6 & 0 & 4 & 4 \\ 0 & 2 & 2 & 2 & 0 & 7 & 0 & 4 \\ 3 & 0 & 2 & 2 & 2 & 0 & 8 & 0 \\ 0 & 0 & 0 & 2 & 2 & 2 & 0 & 0 \end{pmatrix}$$

Figure 7.3: Example of why we need to adjust the Hoshen-Kopelman algorithm to fit the tilted grid. In the left image, purple color indicate flow, and all other links are immobilized, whose cluster sizes we want to color code and count. On the right, the resulting matrix form of the non-modified Hoshen-Kopelman algorithm is shown.

```
IF grid[i][j] == Northeast:
    SET diagonal = grid[i-1][j-1]
ELSE:
    SET diagonal = grid[i-1][j+1]

IF left == 0 and up == 0:
    IF diagonal != 0:
        SET grid[i][j] = diagonal
    ELSE:
        Follow standard procedure of Hoshen-Kopelman

```

By this, we can calculate the cluster distributions for all systems also outside the ground state.

7.1.3 Evolution of cluster sizes

The cluster size distributions for different flow rates are shown in Figure 7.4, and indicates that there will still be a power-law relation, but with a cut-off size, S_0 becoming smaller and smaller for increasing flow rate. This result is analogous to the one in the case of an imposed pressure drop, as done in the work of Chevalier and Talon [36], who got the relation

$$S_0 \propto Q^{-\gamma}$$

with $\gamma \in [0.9, 1.2]$, dependent on how they initialized the disorder of the system. In our case, using the pore-network model, we find these values of γ to fit quite well in this transition, shown in Figure 7.4.

This means that our biggest cluster of immobilized fluid will shrink as flow rate increases, and we know the rate it shrinks with.

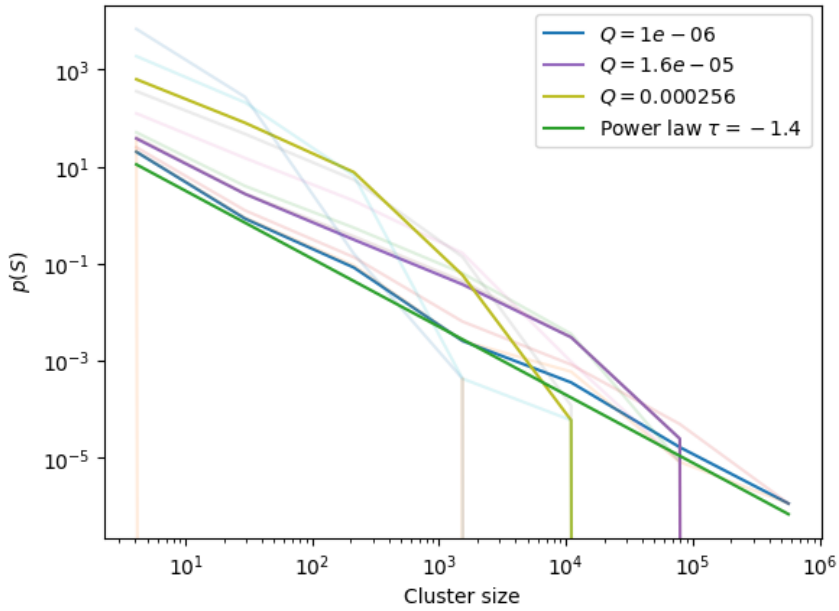

Figure 7.4: Evolution of the cluster power-law distributions as we increase flow rates.

7.2 Scaling of branches

In section 6.2.2 we looked at how many branches we had in the system, and how they scaled with system size – essentially looking at how fast they would merge. This had a clear power-law relation in the ground state, and should evolve into the fully flowing system, where almost all network links are mobilized. The result is shown in Figure 7.5.

We observe that the number of branches in the transition will follow the power-law relation from the ground state for some time, until it stabilizes around some stable number of branches, which we call n_o; this number can be estimated as the number of branches in the outlet row, and is shown in Figure 7.6. This result is important, as it might easily be measured experimentally, and could be a way to separate the yield-stress dominated phases in a phase-diagram, as the exponent is completely independent on system size.

The result of Figure 7.6 clearly indicates a power-law relation here too, with an exponent similar to the merging rate, as discussed in section 6.2.2. Thus we propose the relation $n_o \propto Q^{-\chi}$ with $\chi \approx 2/3$ to hold for predicting the stable number of flowing channels in a Yield Stress fluid flow through a porous medium, in the absence of capillary- and viscous forces.

7.3 Effective permeability of the network

A porous medium will dissipate energy from viscous forces, and determining the amount of energy dissipated is one of the most important large-scale characteristics we could be

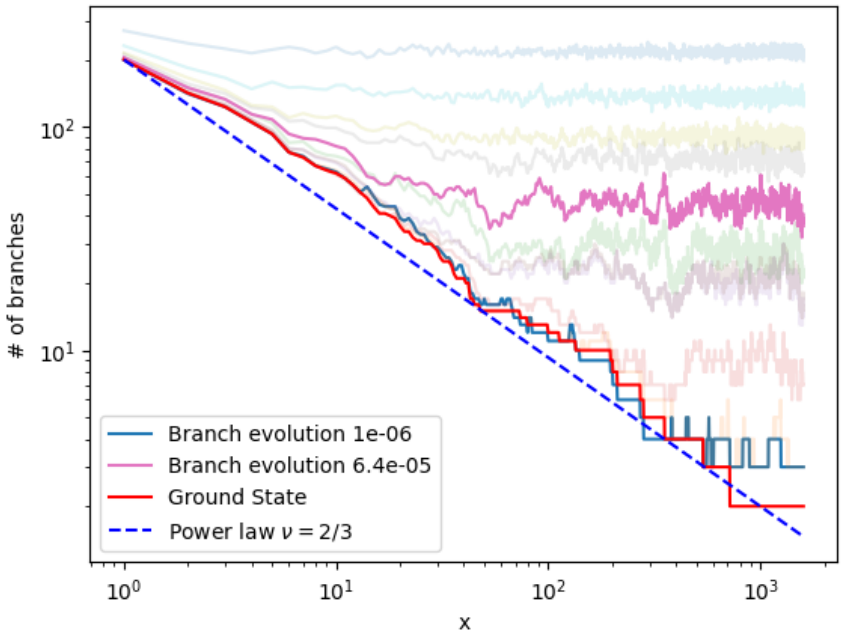

Figure 7.5: Number of branches, as a function of length in the system, shown for different values of imposed flow rates, Q. We clearly see the power-law relation until some cut-off, where the branches merge until the number of branches stabilizes and fluctuates around some value, n_o.

interested in. In a pore-network model this energy dissipation is possible to calculate explicitly in every link, and can be shown to be related to average properties in the system.

It can also be shown that in a system with non-Newtonian fluid, the system will always minimize its energy dissipation, which is used as one of the convergence criteria in the Agumented Lagrangian Method numerical flow solver from chapter 3.3.

Based on non-Newtonian pipe flow, we have the simplified flow equation (derived in equation (3.15)) as

$$\delta p = -(\frac{1}{\sigma}q + \frac{\tau q}{|q|})$$

Now, we can multiply with the current q_{ij} in the link on both sides, and sum over the whole system

$$\sum_{i,j} \delta p_{ij} \cdot q_{ij} = \sum_{i,j} \frac{1}{\sigma_{ij}} q_{ij}^2 + \tau_{ij}|q_{ij}|.$$

Now, on the left hand side, we may simply sum the pressures over the whole system as the total system pressure difference $\langle P_{in} - P_{out} \rangle$, again equal to ΔP multiplied with the macroscopic imposed flow rate Q. The second term in the right hand side can also be

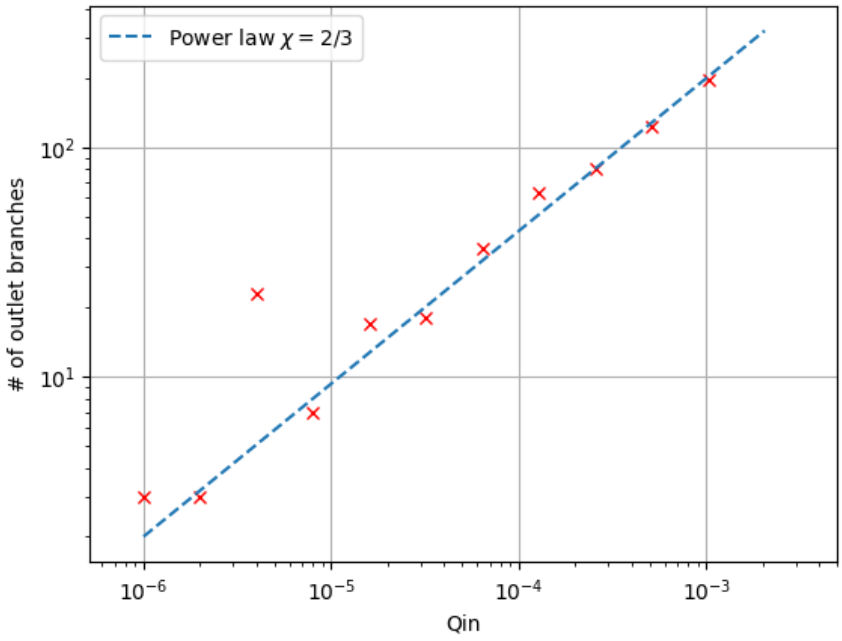

Figure 7.6: Number of outlet branches for different flow rates in the system, as an estimation for the stable number of branches, n_o.

rewritten as the theoretical system threshold pressure ΔP_c[1]

$$Q_{in} \cdot < P_{in} - P_{out} >= Q_{in} \cdot \Delta P = \left(\sum_{i,j} \frac{1}{\sigma_{ij}} q_{ij}^2\right) + \Delta P_c \cdot Q_{in}. \tag{7.1}$$

Finally, we introduce the concept of the effective permeability. This is based on Darcy's equation, written in equation (2.1), and is the phenomenological proportionality constant introduced by Darcy. We write

$$Q = \frac{k_{eff}(Q)}{\nu}(\Delta P - \Delta P_c) \tag{7.2}$$

and insert into the LHS of equation (7.1):

$$Q(\Delta P - \Delta P_c) = Q^2 \frac{\nu}{k_{eff}}$$

and inserting this generalized Darcy law leaves us with the relation for the effective permeability

$$\frac{\nu}{k_{eff}} = 1/Q^2 \sum_{i,j} \left(\frac{1}{\sigma_{ij}} q_{ij}^2\right) \tag{7.3}$$

[1]Note the subtle difference between ΔP_c, which is the yield pressure associated to our particular state S, while P_{th} is the limit of the smallest theoretical system yield pressure, associated to the ground state GS.

The effective permeability of the system can thus be measured by equation (7.3), by calculating this energy dissipation term for systems in various flow rates.

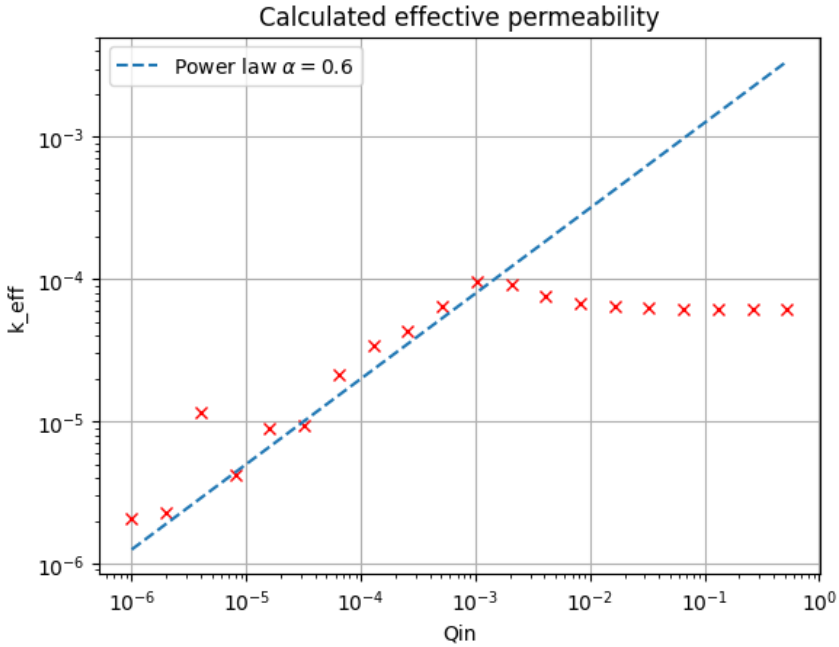

Figure 7.7: Effective permeability of the system in the transition, calculated by equation (7.3).

We calculate the energy dissipation term – of course minimized in the ground state – and plot the effective permeability for different flow rates in Figure 7.7 find another power-law relation, but this one with a clear cut-off at $Q \approx 10^{-3}$, where it flattens out and becomes constant – independent of the flow rate.

In an argument in the introduction, the effective conductivity of the system should change when channels are opening – now it is possible to show how these scale. If we count the number of links that are yielded in the system we find that it scales linearly with flow rate: $d\mathcal{N} \propto dQ^1$ until some cut-off where all links are yielded, as seen in Figure 7.8. However, it also shows that the conductivity of the system will not change linearly with the opening of paths, but rather in the power law

$$d\Sigma \propto dQ^{\alpha} \propto d\mathcal{N}^{\alpha},$$

with $\alpha = 0.6$.

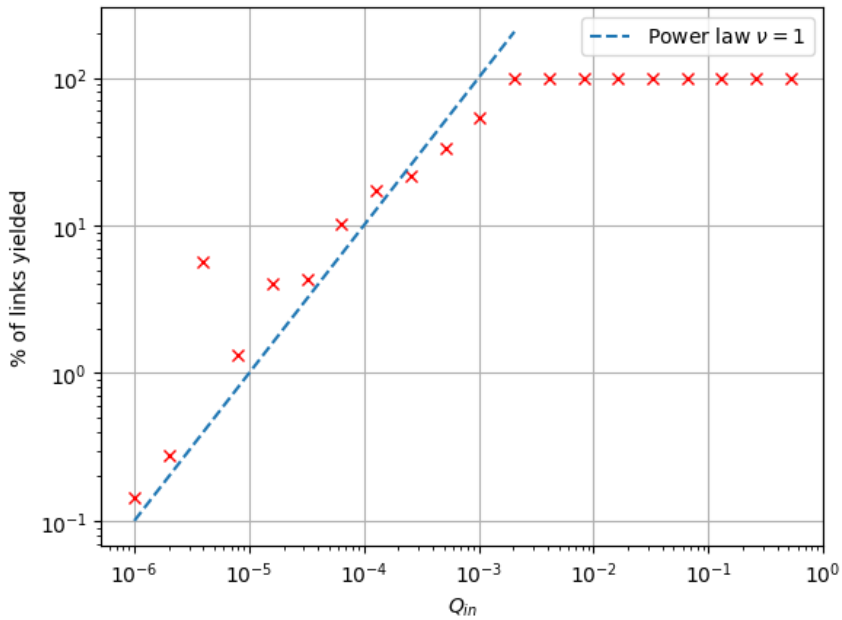

Figure 7.8: The fraction of the system overcoming the local yield pressure for different flow rates in the transition.

8

Exploring Two-Phase Bingham Flows

The framework for understanding two-phase flows with Bingham fluids has been laid in the previous chapters, with a few ways to quantitatively analyze the flow system. We know the limit cases when we only have the yield stress effects, and can now start to look at how the capillary and viscous forces will effect the yield-stress dominated flows, moving one step closer to understanding them in the context of single-phase flows.

8.1 Varying the Yield Number

In equation (3.23) we defined the dimensionless number, expressing the ratio of yield stress to capillary forces as

$$N_\tau = \frac{\tau_c \cdot R}{\sigma},$$

and saw some of its effects qualitatively in Figure 3.5. To move a step further into understanding the complex two-phase flow phenomena, we start looking at the system with equal viscosities $M = 1$, and look isolated on the effect of capillary forces.

A sanity check to start off with: the high-N_τ-limit should force the Newtonian invading fluid to move inside the already open channels, as the immobilized channels will demand a very high pressure to yield. The opposite would be the low-N_τ-limit, where the yield stress effects should be negligible compared to the capillary effects; in total, this limit should give something comparable to the Newtonian phase diagram at $\log M \to 0$ and capillary number increasing with the flow rate: by looking at the phase diagram in Fig. 2.4, we see the flow pattern should go from capillary fingering to a stable displacement in this low-yield limit.

In order to start understanding how the capillary forces couple with the yield stresses, we start off with the high-N_τ-limit, introducing a very small value for σ. Now, the most important effect here will not be the prescence of the capillary forces, but merely the

abscence of the yield stresses in the invading fluid. Even though the viscosity is the same, it is far easier for the invading fluid to push through the channels that are already filled with Newtonian fluid, and hence we expect to see fewer channels. This is indeed what we observe in Figure 8.1, where we observe that the invading fluid will flow sideways (thus also backwards – against the flow rate, due to the 45 degree tilted grid structure). This flow pattern sustains until the capillary number increases sufficiently, where there will be enough force in the flow to open more channels. The single invading tip can be accurately predicted as the single channel with least resistance, which is the exact same behavior as we see when imposing a pressure difference [36].

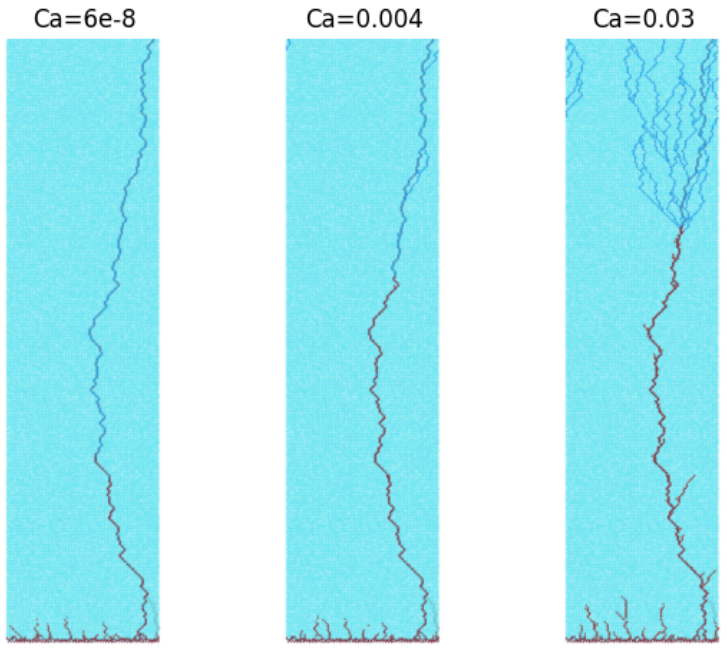

Figure 8.1: Resulting invasion patterns for 3 different capillary numbers with $N_\tau = 200$ and an equally viscous invading fluid, $M = 1$, making it close to being a fully yield-stress dominated flow.

One interesting observation is the pattern we see after the tip of the invading fluid. In some cases, there is only one open channel, while in other cases there will be a branching, seemingly to a certain number of fixed channels. This is reminiscent of the stable number of branches in the transition, seen in Figure 7.6, and backs up our belief that there will be a stable amount of branches, n_0, scaling with the imposed flow rate of the system. Figure 8.1 show that the flow will prefer to merge into the one invading tip, then spreads out when pushing the defending phase.

What we see is that as the paths merge, as we saw in the low-capillary regime, the channels will merge at a greater rate than the one observed in the single-phase systems. After the tip, the number of branches increases rapidly, stabilising to some value. This is exactly the same behavior as in the single-phase case, and we expect to see the same

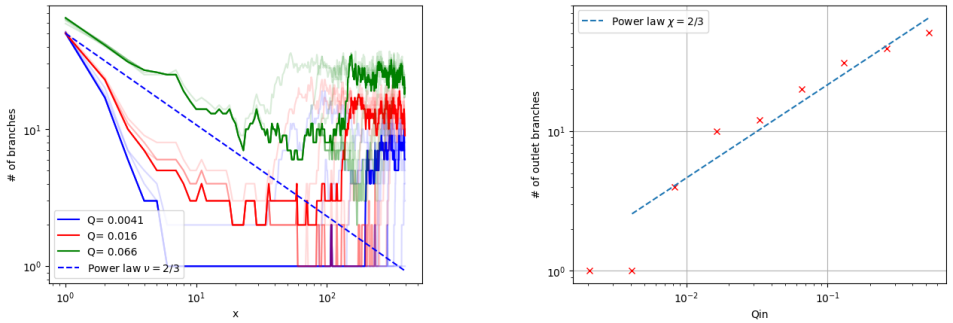

Figure 8.2: Left: Evolution of branches in the system for 3 selected flow rates, evolving with time. The branches merge initially, generally with a higher rate than the observed power-law in Figure 7.5, before increasing after the tip. These simulations had the yield number $N_\tau = 2$ and vicosity ratio of $M = 1$. Right: Number of outlet branches at a selected intermediate time in each simulation, with the associated power-law relation, matching with the findings from single-phase flows (see Figure 7.6.

power-law hold in this case too. Indeed the number of stably flowing branches even in the two-phase flow can be predicted only by the flow rate and the proportionality constant, for all times, as seen in Figure 8.4.

When exploring lower values of N_τ, where the capillary forces are more prominent, we find some completely different patterns. We start seeing the more typical capillary-dominated patterns, making a very interesting interplay that are not presently understood nor has it been properly studied before. Figure 8.3 show us 4 simulations with equally spaced (logarithmically) capillary numbers from one another, illustrating the transition from a capillary- and yield stress dominated flow to a more familiar stable displacement pattern.

Especially the case of $Ca = 0.001$ attracts our attention, as we see it has formed a lot of immobilized clusters, whose distribution may be compared to the ones we found in the single-phase cases. We do not necessarily expect the distributions to match, but it may be interesting in a further work to thoroughly explain the comparison. In the case of this simulation $Ca = 0.001$, we find the PDF of the cluster sizes, shown in Figure 8.4, where we found a different exponent in the power-law relation (6.8).

8.2 Varying the viscosity ratio

Finally, we may also look on the effect of varying the viscosity ratio, and how varying this ratio effects a system with a high yield stress. We also choose to set $\sigma = 0$, totally eliminating the capillary forces, isolating the viscosity effect only.

It might not be surprising, but for a less viscous invading fluid ($M < 1$) we will have the exact same qualitative behavior as in Figure 8.1: one open channel, with the flow going sideways directly to the path of least resistance. Indeed, this behavior will continue until we increase the viscosity and flow rate sufficiently, such that the viscous forces are

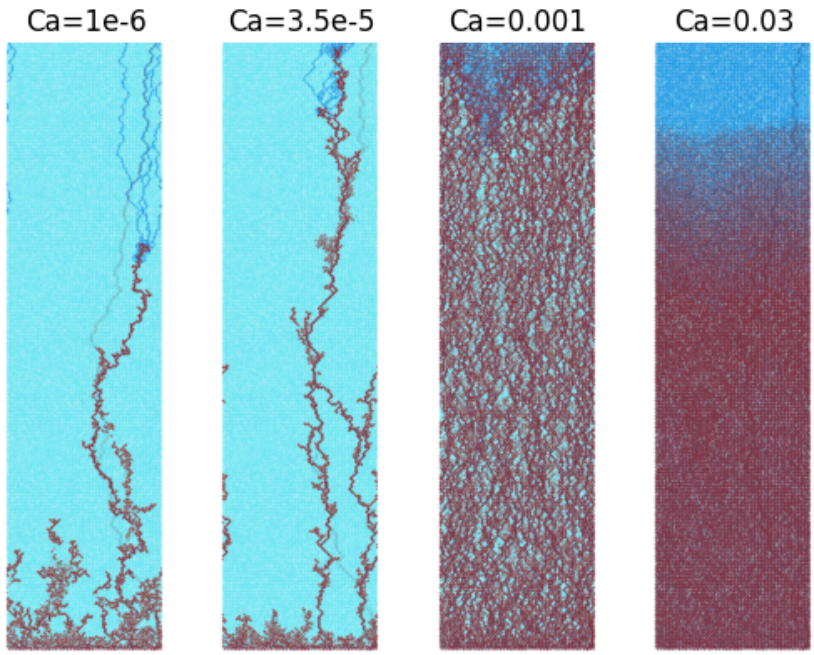

Figure 8.3: Resulting invasion patterns for 4 different capillary numbers with $N_\tau = 0.02$ and an equally viscous invading fluid, $M = 1$.

comparable to the yield pressures. In this case, we will have flows again resembling our defined ground state and transition, as we see in Figure 8.5.

Then the question arises: will this system with a high viscosity ratio, without capillary forces actually be similar to the ground state? Here, it turns out, it does. For instance, the number of branches in the transition was found to obey a power-law, merging at a fixed directed rate, until a cut-off where it found a stable number of branches. We find the same relation for these 3 simulations, shown in Figure 8.6. Unfortunately, due to time constraints, we were not able to follow up on whether this will hold for higher values of imposed flow rate, and even whether it will make sense when switching on the capillary forces. These are left as unanswered questions in this very unexplored territory – a task fit for adventurous souls in the future.

This result proves the utility and importance of actually defining these parameters, and will certainly motivate in finding the total phase-diagram of the Bingham fluids in porous media flows.

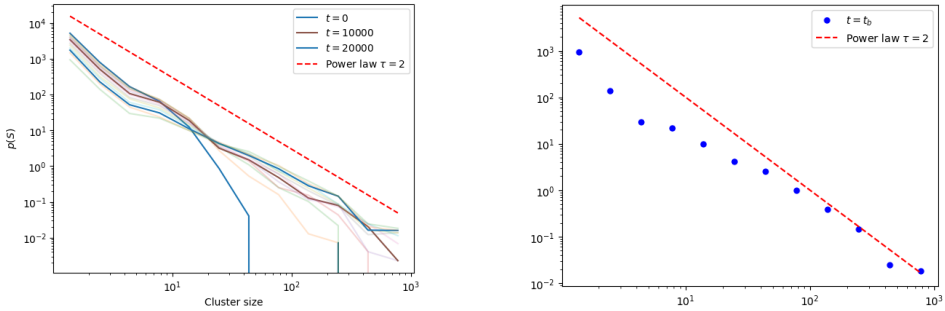

Figure 8.4: Left: Distribution of immobilized clusters for a set of different times in the simulation, showing the power-law exponent to be $\tau \approx 2$ in the equation (6.8). Right: The distribution at the breakthrough time t_b, showing that this distribution will not be well described with a power-law close to the breaktrhough – as time evolves the ratio of large-sized clusters to small-sized clusters will increase.

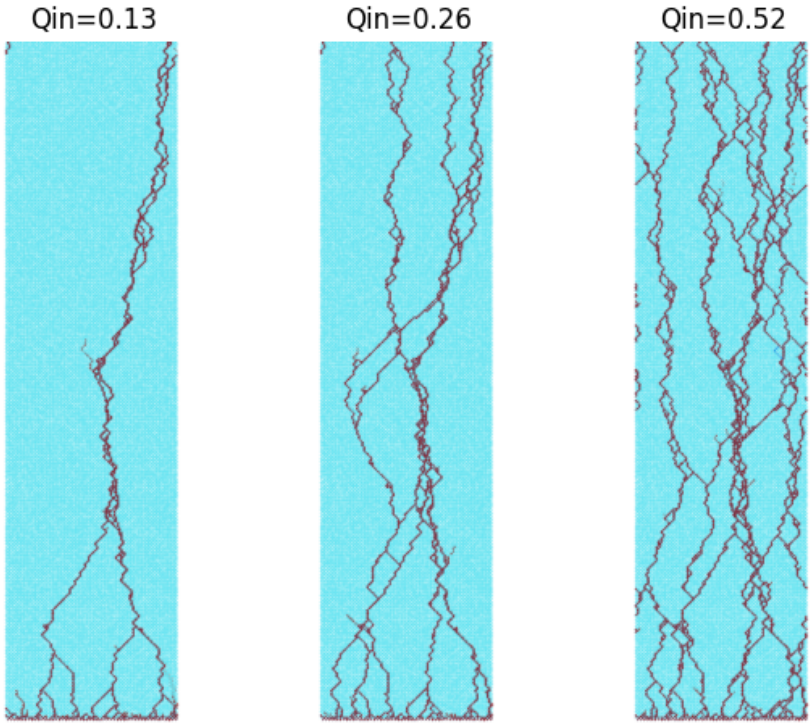

Figure 8.5: Resulting invasion patterns for 3 different imposed flow rates when capillary forces are switched off, with $M = 100$, making the vicous forces comparable to the yield stresses. Note the similarity to the transition from chapter 7. All 3 images show the breakthrough pattern, $t = t_b$.

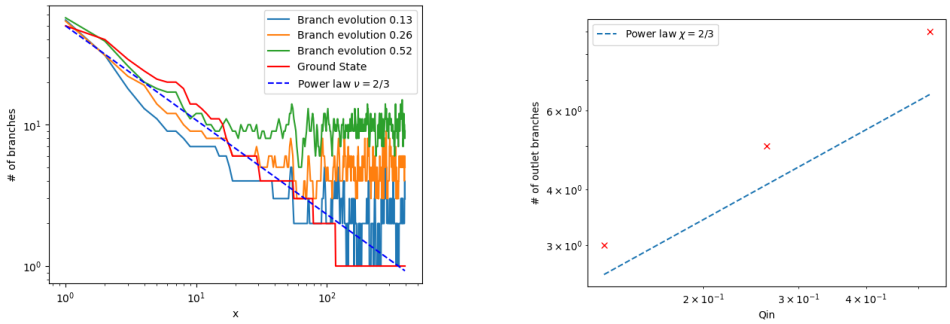

Figure 8.6: Left: Evolution of the branches at breakthrough $t = t_b$, following the exact same behavior as the transition for single-phase Bingham flows. Right: The number of outlet branches, seemingly also being described with the same power-law relation.

9

Conclusions and further work

In this Master's thesis, a pore network model was implemented to work on non-Newtonian rheologies with a recently developed Agumented Lagrangian Method. The simulator consists of a set of quite simple rules, and enabled us to look further into the complex and unexplored field of Bingham fluids in porous media, even in a two-phase system. However, due to the complexity of all the physical rules and principles present in these flows, we decided to look further into single-phase flows with Bingham fluids.

This was done for several reasons, mainly to isolate one effect and study its effect in isolation. The main feature of these single-phase Bingham fluids in porous media was the region where the imposed flow rates went to 0, where we saw a transition that exhibited non-Darcy behavior, $Q \propto (\Delta P - \Delta P_{th})^{\beta}$ with $\beta \neq 1$. This was studied earlier by Talon [36, 33, 34], among others, for an imposed pressure difference, who also proved the non-Darcy properties; an interesting find we did was another power-law exponent β in the Darcy relation for our imposed *flow rate* than they did with an imposed *pressure difference*, making the power law dependent on the boundary condition.

We thus studied this transition with imposed flow rate further, finding a connection to high-T_c superconductors from the work of Drossel and Kardar [23]. The underlying mechanisms were described as directed polymers, and led us to define a ground state for the single-phase flow system. This was studied, and proved able to predict the exact value of P_{th} only from knowing the link radii and the rheology of the fluid – no simulations or fits were needed to find this total threshold pressure.

We also found the number of branches, evolving along the flow direction, merging at a certain rate, determined by a power law with exponent $n(x) \propto x^{-2/3}$. The clusters of immobilized fluid were another characteristic feature of these single-phase systems, where we found their lengths and sizes following clear power-law relations too. These are the limit cases of $Q \to 0$ and $\tau_c \to \infty$, and has clear signs we can look for in order to understand the impact of this yield stress.

The systems in the transition proved to exhibit the same kinds of power-law relations, but in this case with a cut-off at some point, both for the probability density in the cluster sizes and in the evolution of branches, expressing that the system's biggest immobi-

lized cluster shrinks with increased flow. This proved to predict the number of preferred branches, n_0 , which the system will fluctuate around after stabilizing. The effective permeability of the flow in the transition was possible to calculate, and proved to increase from the ground state to the fully flowing case. This is the most interesting macroscopic property of a porous media flow, and has not been covered in the existing literature, as far as we know.

These properties were again explored for some limit cases in a two-phase Bingham flow, finding explanations for how the yield stress will effect these complex systems. Indeed, number of branches and sizes of clusters were used to see whether the two-phase flow had any similarities to the more understandable single-phase Bingham flows, and it turned out that we observe patterns very similar to the transition from ground state to fully mobilized system when the viscosity of the invading fluid was higher than that of the Bingham fluid.

There are so much to do further in this field, and we really have just scratched the surface of all there is to come. With so much complexity and force competitions, there are still possibilities of finding completely new phases to add into a total phase-diagram of yield stress fluids in porous media. The link up to statistical physics might continue to prove useful, and may provide more interesting similarities, like the similarity to type-II superconductors. KPZ-theory may be a promising place to start, and from all this, we may find utility and applications for both single- and two-phase flows with Bingham fluids. This is a field in its earliest stage, and with todays algorithms and computational prowess, only the sky is the limit.

Furthermore, comparing the pore-network simulations to real experimental data would be important for validation of these findings. One could also expand the work into index fluids, adding the effect of shear-thinning and shear-thickening in the yield stress fluids.

Part III

Appendices

(Project and Master theses)

Appendix

A Initial experimental results

Over the duration of this project, we also conducted a series of experiments for comparing with the simulations. These follow the same structure and setup as [39], among others, and will be briefly explained in this appendix.

The experiments were conducted with Federico Lanza and Khoubaib Khoubaib, who deserve the extra acknowledgement for the help in doing this work.

Porous media sample

The sample of a porous media used in the experiments are 3D printed transparent flat Hele-Shaw cells with circular beads randomly packed inside to mimic a porous structure. Such a model is made by programming the bulk by placing circles of random radius (drawn from a specified distribution) in random positions where there are no other circles colliding. In this procedure, one can calculate the porosity (ratio of pore volume to material volume) of the material, as well as finding the theoretical minimal threshold path (see equation (3.24)), which could be compared to the actual experiment in a future work. On the top and the bottom of the sample, we put a layer of PVC and tighten to prevent any fluid from leaking out. Inlets and outlets on the opposite sides are connected to the sample with a small mixing chamber on the inlet rows, to prevent one particular inlet to be preferred, avoiding local effects.

The inlet rows is then connected by tubes to the pump (Standard PHD ULTRA™ CP Syringe Pump) working as the controlling driving force of the flow. The pump controls the imposed flow rate, and is therefore useful for comparing the experiments to the simulations. The outlets of our sample is simply open tubes, setting a constant pressure.

Experimental setup

The experimental setup is shown in figure The sample is laid flat on top of a light-box, adjusted with a digital goniometer to ensure the incline never exceeded 0.15° to safely negate the gravitational forces. The transparent sample is then photographed with a digital camera placed directly above by a tripod. The pictures are taken with a set time interval, adjusted to have sufficient time resolution on the experiments. We want to measure the behavior of a yield stress fluid, and as we mentioned in chapter 3, the Bingham fluid is just the idealization of a fluid with yield stresses. In our case, we used a mixture of carbopol powder and tap water as our yield stress fluid (wetting phase), which has the additional property of being shear-thinning (thus having a rheological relation as case (c) in Figure 3.1). Finally, we dye the carbopol black, and use air as the invading fluid, making it very easy to separate the two phases in the resulting images. The same setup is used for all experiments, and runs until we have breakthrough in the nonwetting (air) phase, i.e. the air has formed a channel all the way through from the inlet to any outlet.

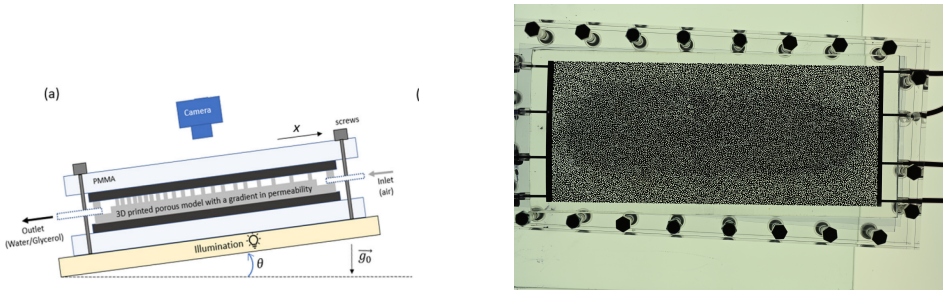

Figure 9.1: Left: Illustration of the commonly used experimental setup, in this case also controlling the incline. Image courtesy of [39]. Right: Example image from the camera before the invasion starts.

Data analysis

After acquiring the images from the simulations, we use a python-script to analyze the time-evolution of the growth pattern. The goal is to make spatio-temporal plots, similar to a rectangular version of the ones presented in Eriksen et al. [19], and in order to do this, some image processing is required. In our case we use the Matplotlib Image library, as well as some functions from Scipy and SKImage.

First off, we know that any dark pixel in the sample must be the yield stress fluid, while the light pixels are either pore cylinders or the injected air. The first thing we do is then to binarize the image. All pixels will have a value between 0 and 255, so we set all values below the threshold to be 0, and all values above to be 255 – making a clear black and white image of the image. Then, we select an image taken before the experiment has started, denoted t_0, and use this to find the difference between t_0 and each image taken in the experiment. In this way, we are able to track each pixel, and determine at what time-step it will go from black to white, with a python example code:

```
# Python example:
img_ini = image.imread('frame_00003.jpg')[200:3700 ,1200:4500, :]
img_current = image.imread('frame_00073.jpg')[200:3700 ,1200:4500, :]

threshold = 165 #Out of 255
b_ini = 255*(img_ini>threshold)
b_current = 255*(img_current>threshold)

b_diff = b_current - b_ini

```

When doing such experiments, one cannot make sure the camera will remain absolutely still. Vibrations in the room will make the camera move ever so slightly, which ends up looking like noise in the final image. One way to adjust for this is to calculate the spatial correlation function between our image and the initial image at $t = 0$, giving us the offset between the two. A correlation function is computationally expensive to calculate, so we select one window in each of the two pictures, and offset the current image so that it fits with the background. There will still be some noise, and although there are several other ways to remove this noise, we clearly see the invasion pattern, making it possible to

qualitatively compare to the simulation data.

Spatio-temporal results

An example of a Spatio-temporal result is shown in Figure 9.2, where we see the directedness of the air invasion, as explained in the case of a lower viscosity invasion in the simulations in chapter 8. With the information of the rheological properties in the defending yield stress fluid, these kinds of results may quantitatively be compared to the simuations.

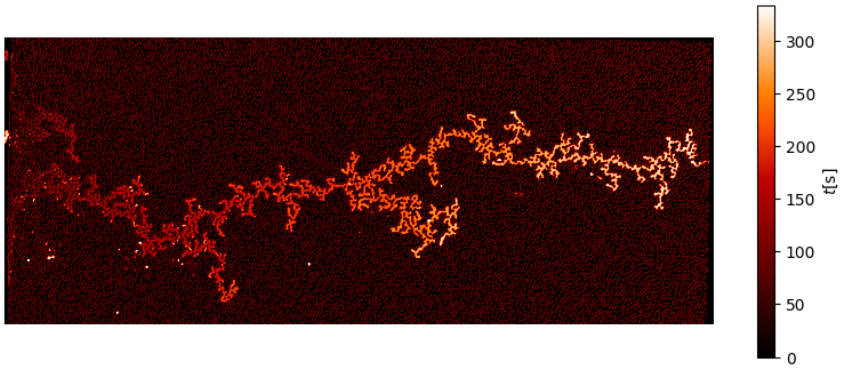

Figure 9.2: Resulting spatio-temporal plot of the invasion pattern, with time on the z-axis.

A qualitative comparison can still be made, and the resulting invasion pattern resembles the ones we find in the high $N_t au$-region in Figure 3.5. The effect of the camera vibrations can be seen in the grainy background, even after running the correlation-function algorithm to find the offset and adjust for the vibrations.

Lack of viscosity measurements

The main reason these experiments are in an appendix instead of in the main text, is the lack of the rheological properties of the carbopol solution, making it impossible to say where in the phase diagram we would be. We don't know neither the viscosity nor the yield stress, making it hard to conclude with anything. An effort was made to measure the viscosity with a quite simple experiment, making a rough estimate for Newtonian fluids and can be used to find a fit for the non-Newtonian rheology. The setup consists of some simple tubes with a known radius, along with a pump that provides a constant known flow rate Q. By then setting two tubes vertically with one horizontal connecting them, one can estimate the net pressure drop over the tube horizontal tube of length L, as the difference in the hydrostatic pressures in the vertical tubes, measured as

$$\Delta P = \rho g h_1 - \rho g h_2 = \rho g(\Delta h).$$

This must be equal to the pressure drop in the tube, calculated by the Poiseuille law:

$$\Delta P = \frac{8\nu L}{\pi r^4} Q$$

Combining these two expressions for the pressure drop leaves us with the final expression for the viscosity:

$$\nu = \frac{\pi \rho g r^4}{8QL} \Delta h$$

Hence, only the fluid heights in the vertical tubes is the only thing that needs to be measured.

However, the experiment did not work properly in our case of the yield stress, leading to no concluisions on the rheology of the carbopol solution. The rheological relation is usually measured by a rheometer, by measuring the forces in a circular Couette flow.

B Presentation of this work on the InterPore 2023 conference

Pore-Network Simulations of Yield Stress Fluids in Porous Media

Andreas Hennig[1], Federico Lanza[1,3], Laurent Talon[2], Alex Hansen[1], Alberto Rosso[3]

[1] PoreLab, Department of Physics, Norwegian University of Science and Technology, N-7491 Trondheim, Norway
[2] FAST, CNRS, Université Paris-Saclay, 91405 Orsay, France
[3] LPTMS, CNRS, Université Paris-Saclay, 91405 Orsay, France

Norwegian University of Science and Technology

NTNU

PoreLab
NTNU-UiO Porous Media Laboratory

Introduction

- What is a Yield Stress Fluid?
- Applications in engineering problems like ground reinforcement

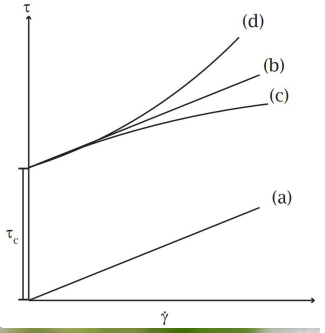

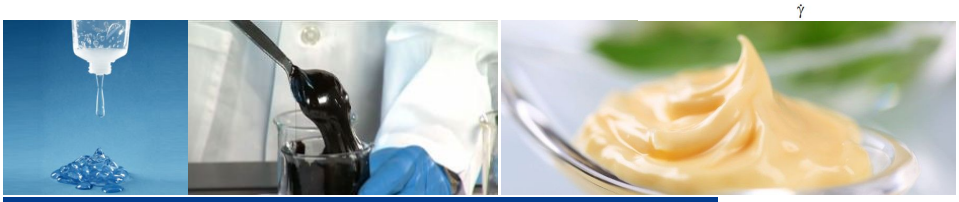

2 NTNU

Darcy's law for Bingham fluids

Chevalier T, Talon L. Phys Rev E Stat Nonlin Soft Matter Phys. Feb;91(2):023011. 2015.

- Single phase flow with imposed pressure
- Able to predict the minimal pressure to have flow in the system: ΔP_c
- Link to newtonian two phase flows

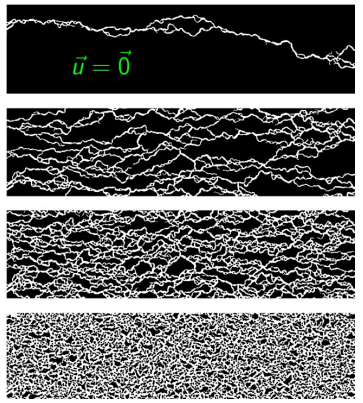

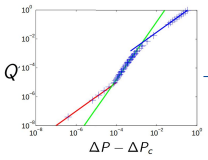

3 scaling regimes:-
- $Q \propto (\Delta P - \Delta P_c)^1$
- $Q \propto (\Delta P - \Delta P_c)^2$
- $Q \propto (\Delta P - \Delta P_c)^1$

Imposing flow rate

Figure coloring:

- Red – Invading fluid
- Light blue – Immobilized defending fluid
- Dark blue – Flowing defending fluid
- Grey line – Path of least resistance

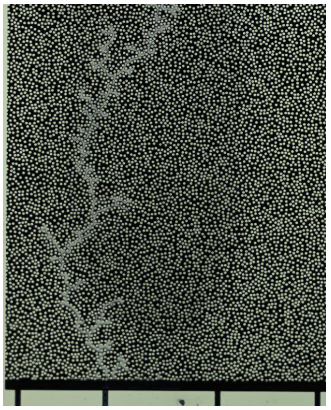

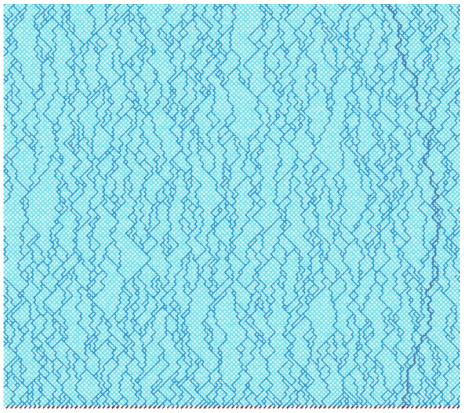

Pore Network model

- Idea: Model a porous media as a network of tubes in a regular grid
- Implemented with the bubble mechanics from Sinha et al. Front. Phys. 8:548497, 2021

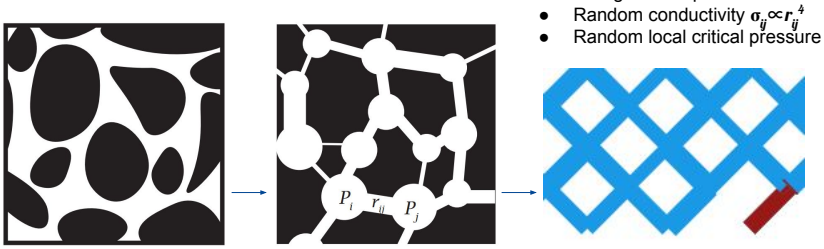

- Equal tube length l
- Hourglass-shaped tubes
- Random conductivity $\sigma_{ij} \propto r_{ij}^{4}$
- Random local critical pressure $\tau_{ij} \propto r_{ij}^{-1}$

Augmented Lagrangian method

L.Talon and A.Hansen, Front. Phys 7:225, 2020

- Impose nonlinear Poiseuille flow in the tubes
- Need to solve a coupled nonlinear system of equations
- Express Kirchhoff condition as Lagrangian multiplier

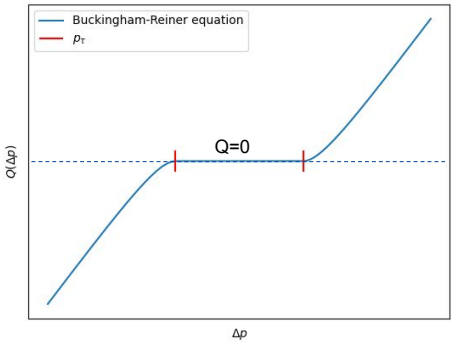

6 NTNU

Transition from single tube into a fully flowing system

- More tubes will open as imposed flow is increased
- Branches will merge, following a clear power-law when Q→0
- Get the same Darcy relation

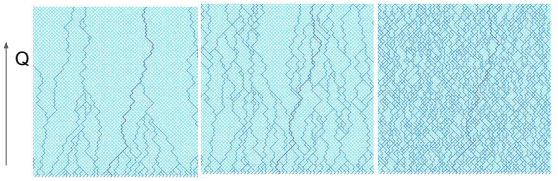

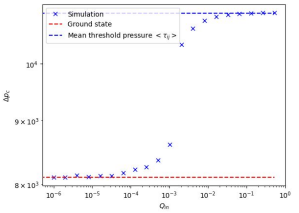

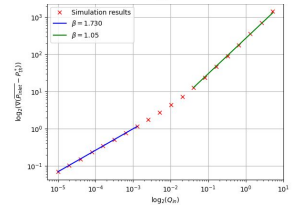

Permeability in the transition

- By evaluating the energy dissipation in each tube, we can express an effective permeability
- Permeability follows a power law with exponent 0.6

$$\delta p = -(\frac{1}{\sigma} q + \frac{\tau q}{|q|})$$

$$\sum_{i,j} \delta p_{ij} \cdot q_{ij} = \sum_{i,j} \frac{1}{\sigma_{ij}} q_{ij}^2 + \tau_{ij} |q_{ij}|$$

$$Q_{in} \cdot < P_{in} - P_{out} >= \left(\sum_{i,j} \frac{1}{\sigma_{ij}} q_{ij}^2 \right) + \Delta p_c(Q_{in}) \cdot Q_{in}$$

$$Q_{in}(\Delta p - \Delta p_c(Q_{in})) = \sum_{i,j} (\frac{1}{\sigma_{ij}} q_{ij}^2) = \frac{k_{eff}(Q_{in})}{\nu} Q_{in}^2$$

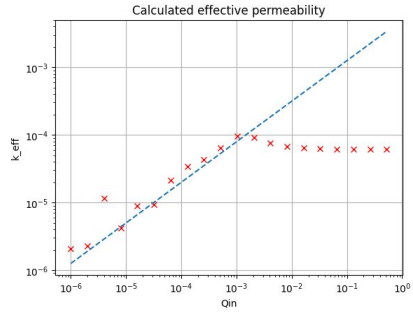

Relation to statistical physics

B.Drossel and M.Kardar, Phys. Rev. E 52:4841, 1995

Flux lines in superconductors

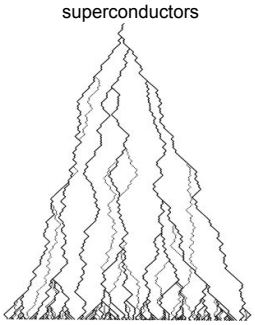

Predicted Ground State

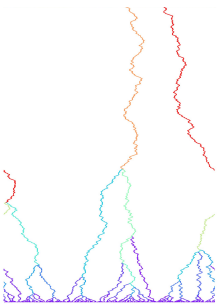

Flow field for low Q

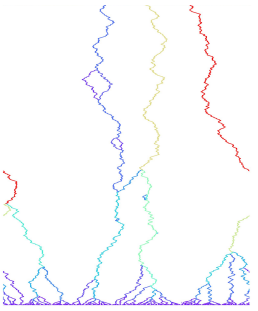

Image from B.Drossel and M.Kardar, Phys. Rev. E 52:4841, 1995

Relation to statistical physics

- Branches follow a clear power-law of -⅔
- Looking at the cluster size distributions we get another power law with exponent 1.4
- These things are still not explained – could we predict these results theoretically?

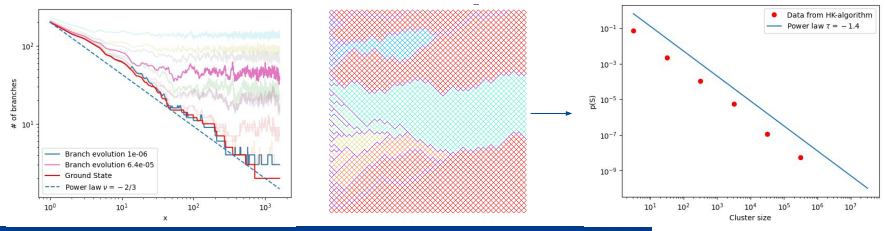

10 NTNU

Bibliography

[1] F. Arbabi, H. Montazeri, R. Abouatallah, R. Wang, and A. Bazylak. Three-dimensional computational fluid dynamics modelling of oxygen bubble transport in polymer electrolyte membrane electrolyzer porous transport layers. *Journal of The Electrochemical Society*, 163(11):F3062, jun 2016.

[2] Mesfin M. Mekonnen and Arjen Y. Hoekstra. Four billion people facing severe water scarcity. *Science Advances*, 2(2):e1500323, 2016.

[3] Martin Fernø. The fluidflower initiative – a physical porous media flow rig for interdisciplinary underground research. In *5th National Workshop on Porous Media*, 2022.

[4] Jens Feder, Eirik Grude Flekkøy, and Alex Hansen. *Physics of Flow in Porous Media*. Cambridge University Press, 2022.

[5] Subhadeep Roy, Håkon Pedersen, Santanu Sinha, and Alex Hansen. The co-moving velocity in immiscible two-phase flow in porous media. *Transport in Porous Media*, 143, 05 2022.

[6] Alex Hansen, Eirik Grude Flekkøy, Santanu Sinha, and Per Arne Slotte. A statistical mechanics framework for immiscible and incompressible two-phase flow in porous media. *Advances in Water Resources*, 171:104336, 2023.

[7] Bessonov, N., Sequeira, A., Simakov, S., Vassilevskii, Yu., and Volpert, V. Methods of blood flow modelling. *Math. Model. Nat. Phenom.*, 11(1):1–25, 2016.

[8] Markus Reiner. *Advanced Rheology*. H. K. Lewis & Co. Ltd., 1971.

[9] Frank M. White and Joseph Majdalani. *Viscous Fluid Flow*. McGraw Hill, 2022.

[10] P. Coussot. Yield stress fluid flows: A review of experimental data. *Journal of Non-Newtonian Fluid Mechanics*, 211:31–49, 2014.

[11] Crystal E. Owens, Max R. () Fan, A. John Hart, and Gareth H. McKinley. On oreology, the fracture and flow of "milk's favorite cookie®". *Physics of Fluids*, 34(4):043107, 2022.

[12] H. Darcy. *Les fontaines publiques de la ville de Dijon: exposition et application des principes à suivre et des formules à employer dans les questions de distribution d'eau.* Victor Dalmon, 1856.

[13] Roland Lenormand, Eric Touboul, and Cesar Zarcone. Numerical models and experiments on immiscible displacements in porous media. *Journal of Fluid Mechanics*, 189:165–187, 1988.

[14] Chen Liu, Andrea De Luca, Alberto Rosso, and Laurent Talon. Darcy's law for yield stress fluids. *Phys. Rev. Lett.*, 122:245502, Jun 2019.

[15] Santanu Sinha, Magnus Aa. Gjennestad, Morten Vassvik, and Alex Hansen. Fluid meniscus algorithms for dynamic pore-network modeling of immiscible two-phase flow in porous media. *Frontiers in Physics*, 8, 2021.

[16] Franziska Moebius and Dani Or. Interfacial jumps and pressure bursts during fluid displacement in interacting irregular capillaries. *Journal of Colloid and Interface Science*, 377(1):406–415, 2012.

[17] Senyou An, Hamidreza Erfani, Omar Godinez-Brizuela, and Vahid Niasar. Transition from viscous fingering to capillary fingering: Application of gpu-based fully implicit dynamic pore network modeling. *Water Resources Research*, 56, 12 2020.

[18] Jens Feder. *Fractals*. Physics of Solids and Liquids. Springer, 1988.

[19] Fredrik K. Eriksen, Marcel Moura, Mihailo Jankov, Antoine L. Turquet, and Knut J. Måløy. Transition from viscous fingers to compact displacement during unstable drainage in porous media. *Phys. Rev. Fluids*, 7:013901, Jan 2022.

[20] R. Kostenko and L. Talon. Numerical study of bingham flow in macroscopic two dimensional heterogeneous porous media. *Physica A: Statistical Mechanics and its Applications*, 528:121501, 2019.

[21] Min Chen, William Rossen, and Yannis C. Yortsos. The flow and displacement in porous media of fluids with yield stress. *Chemical Engineering Science*, 60(15):4183–4202, 2005.

[22] Laurent Talon and Alex Hansen. Effective rheology of bi-viscous non-newtonian fluids in porous media. *Frontiers in Physics*, 7, 2020.

[23] Barbara Drossel and Mehran Kardar. Scaling of energy barriers for flux lines and other random systems. *Physical Review E*, 52(5):4841–4852, nov 1995.

[24] S. Roux and H. J. Herrmann. Disorder-induced nonlinear conductivity. *Europhysics Letters*, 4(11):1227, dec 1987.

[25] Santanu Sinha and Alex Hansen. Effective rheology of immiscible two-phase flow in porous media. *Europhysics Letters (epl)*, 99, 02 2012.

[26] Federico Lanza. Two-phase non-linear flow in pore network model. In *Interpore 2023*, May 2023.

[27] Santanu Sinha. Disorder-induced non-linearity in the growth of viscous fingers. In *Informal Workshop on Upscaling*, May 2023.

[28] Mehran Kardar and Yi-Cheng Zhang. Scaling of directed polymers in random media. *Phys. Rev. Lett.*, 58:2087–2090, May 1987.

[29] J E Green and M A Moore. Application of directed lattice animal theory to river networks. *Journal of Physics A: Mathematical and General*, 15(11):L597, nov 1982.

[30] Antonio Rodríguez de Castro, Abdelaziz Omari, Azita Ahmadi-Sénichault, and Denis Bruneau. Toward a new method of porosimetry: Principles and experiments. *Transport in Porous Media*, 101, feb 2014.

[31] Martin Lanzendörfer, Soheil Safari Anarkouli, Martin Slavík, Jan Najser, and Jakub Roháč. Measuring the changes in the pore size distribution of a soil sample during its compression using non-newtonian fluids. 05 2023.

[32] Victor Francia, Lyes Ait Ali Yahia, Raffaella Ocone, and Ali Ozel. From quasi-static to intermediate regimes in shear cell devices: Theory and characterisation. *Powder and particle*, 38, 09 2020.

[33] Laurent Talon and Daniela Bauer. On the determination of a generalized darcy equation for yield-stress fluid in porous media using a lattice-boltzmann trt scheme. *The European Physical Journal E*, 36, 12 2013.

[34] Laurent Talon, Harold Auradou, Marc Pessel, and Alex Hansen. Geometry of optimal path hierarchies. *EPL (Europhysics Letters)*, 103:30003, 08 2013.

[35] Alex Hansen and János Kertész. Phase diagram of optimal paths. *Phys. Rev. Lett.*, 93:040601, Jul 2004.

[36] Thibaud Chevalier and Laurent Talon. Generalization of darcy's law for bingham fluids in porous media: From flow-field statistics to the flow-rate regimes. *Phys. Rev. E*, 91:023011, Feb 2015.

[37] L. E. Aragón, A. B. Kolton, P. Le Doussal, K. J. Wiese, and E. A. Jagla. Avalanches in tip-driven interfaces in random media. *Europhysics Letters*, 113(1):10002, jan 2016.

[38] J. Hoshen and R. Kopelman. Percolation and cluster distribution. i. cluster multiple labeling technique and critical concentration algorithm. *Phys. Rev. B*, 14:3438–3445, Oct 1976.

[39] Tom Vincent-Dospital, Marcel Moura, Renaud Toussaint, and Knut Jørgen Måløy. Stable and unstable capillary fingering in porous media with a gradient in grain size. *Communications Physics*, 5(1):306, Nov 2022.

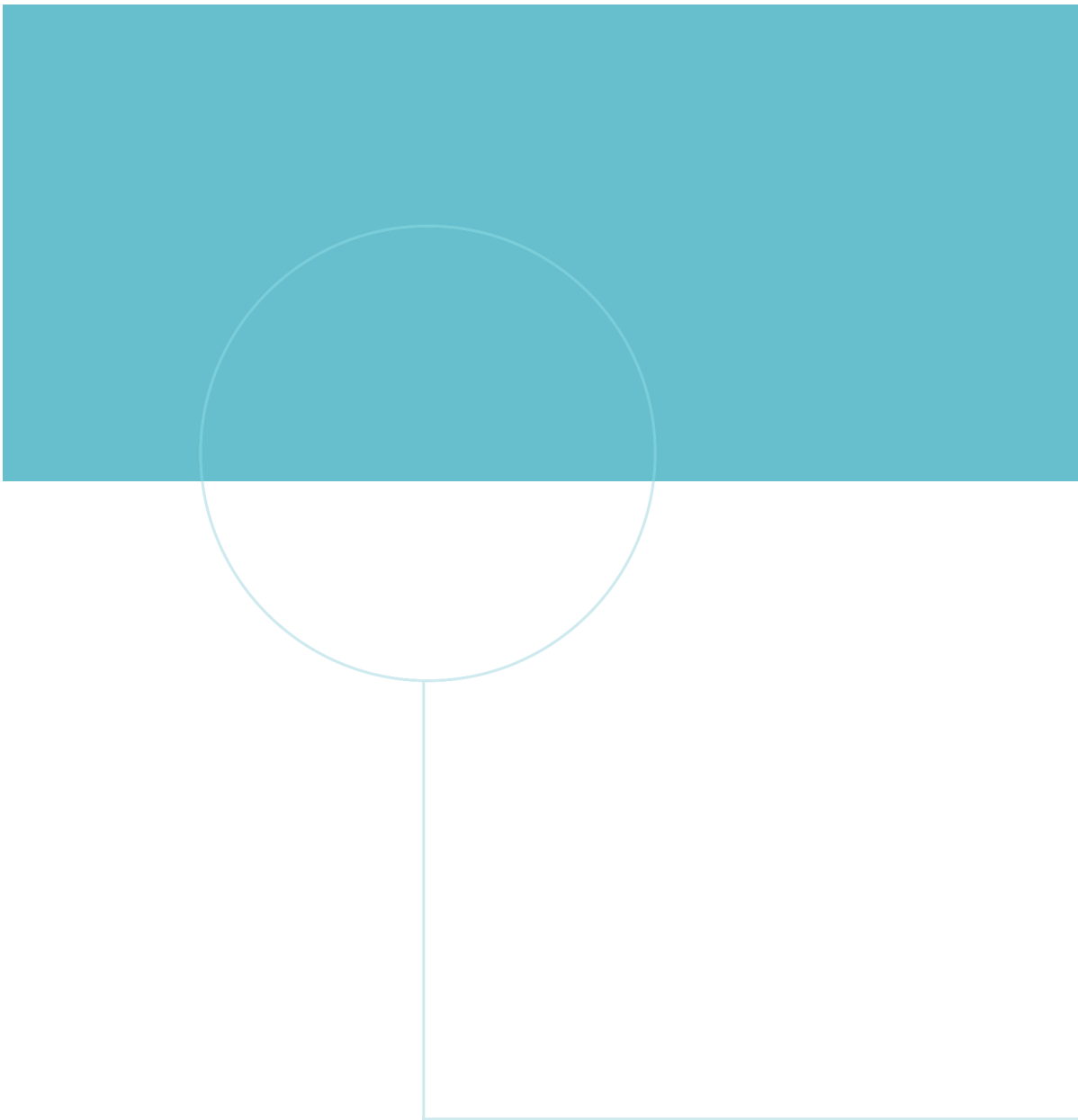

NTNU

Norwegian University of
Science and Technology